

AO-A191 454

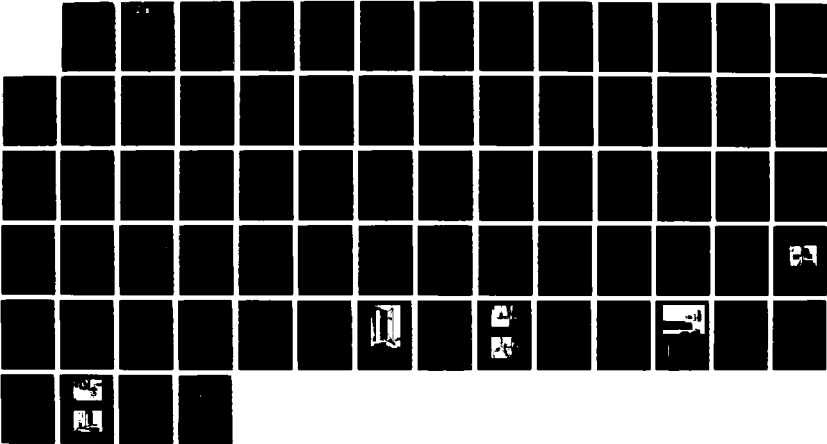
EXPERIMENTAL STUDY OF ACTIVE VIBRATION CONTROL(U)  
VIRGINIA POLYTECHNIC INST AND STATE UNIV BLACKSBURG  
DEPT OF A. W L HALLAUER 31 AUG 87 AFOSR-TR-88-0060  
F49620-85-C-0024

1/1

UNCLASSIFIED

F/G 22/2

NL





DTIC

REPORT DOCUMENTATION PAGE

AD-A191 454

DTIC  
SELECTED  
FEB 25 1988  
H

1b. RESTRICTIVE MARKINGS	
3. DISTRIBUTION / AVAILABILITY OF REPORT Unclassified/Unlimited Approved for public release distribution unlimited	
4b. DECLASSIFICATION / DOWNGRADING SCHEDULE	5. MONITORING ORGANIZATION REPORT NUMBER(S) <b>AFOSR-TR-88-0060</b>

4. PERFORMING ORGANIZATION REPORT NUMBER(S)	5. MONITORING ORGANIZATION REPORT NUMBER(S)
---	---

6a. NAME OF PERFORMING ORGANIZATION Virginia Polytechnic Institute and State University	6b. OFFICE SYMBOL (if applicable) AOE	7a. NAME OF MONITORING ORGANIZATION Air Force Office of Scientific Research/NA
--	--	---

6c. ADDRESS (City, State, and ZIP Code) Dept. of Aerospace and Ocean Engineering VPI&SU Blacksburg, Virginia 24061	7b. ADDRESS (City, State, and ZIP Code) Directorate of Aerospace Sciences Building 410 Bolling AFB, DC 20332
---	---

8a. NAME OF FUNDING / SPONSORING ORGANIZATION AFOSR	8b. OFFICE SYMBOL (if applicable) AFOSR/NA	9. PROCUREMENT INSTRUMENT IDENTIFICATION NUMBER Contract F49620-85-C-0024
--	---	--

8c. ADDRESS (City, State, and ZIP Code) AFOSR/NA Bolling AFB, DC 20332	10. SOURCE OF FUNDING NUMBERS		
	PROGRAM ELEMENT NO. G1102F	PROJECT NO. 2302	TASK NO. B1

11. TITLE (Include Security Classification) Experimental Study of Active Vibration Control
---

12. PERSONAL AUTHOR(S) Hallauer, William L. Jr.
--

13a. TYPE OF REPORT Final Technical	13b. TIME COVERED FROM 86-1-30 TO 87-8-31	14. DATE OF REPORT (Year, Month, Day) 1987 August 31	15. PAGE COUNT 69
--	--	---	----------------------

16. SUPPLEMENTARY NOTATION vibration
---

17. COSATI CODES	18. SUBJECT TERMS (Continue on reverse if necessary and identify by block number) Structural dynamics; structural wave propagation; active vibration damping, active control, experimental modal analysis, large spacecraft structures
FIELD      GROUP      SUB-GROUP	

19. ABSTRACT (Continue on reverse if necessary and identify by block number) Complementary experimental-theoretical studies were conducted on the following subjects related to the dynamics and control of flexible large spacecraft structures: 1) Transient wave propagation: - Extensive results are presented for traveling waves in a laboratory structure excited by suddenly applied oscillatory point forces; 2) The dynamics of a thin-walled grid with a rigid body slewing degree of freedom; - The design, theoretical analysis, experimental testing, and experimental-theoretical correlation are reported. Even after much refinement, the finite element model of the relatively simple structure did not satisfactorily predict the measured dynamic behavior; 3) Active damping and control of the slewing grid with the use of structure-borne accelerometers and reaction wheel actuators: - The results of an active damping experiment are presented. Also discussed are the serious practical problems encountered in this research and the potential for future experiments with simultaneous control of maneuvering and vibration.
---

20. DISTRIBUTION / AVAILABILITY OF ABSTRACT <input checked="" type="checkbox"/> UNCLASSIFIED/UNLIMITED <input type="checkbox"/> SAME AS RPT <input type="checkbox"/> DTIC USERS	21. ABSTRACT SECURITY CLASSIFICATION Unclassified
--	--

22a. NAME OF RESPONSIBLE INDIVIDUAL Anthony K. Amos	22b. TELEPHONE (Include Area Code) 202/767-4937	22c. OFFICE SYMBOL AFOSR/NA
--	--	--------------------------------

FINAL TECHNICAL REPORT  
TO THE AIR FORCE OFFICE OF SCIENTIFIC RESEARCH  
FOR THE PERIOD 30 JANUARY 1986 TO 31 AUGUST 1987

CONTRACT F49620-85-C-0024

EXPERIMENTAL STUDY OF ACTIVE VIBRATION CONTROL\*

William L. Hallauer Jr.  
Department of Aerospace and Ocean Engineering  
Virginia Polytechnic Institute and State University

TABLE OF CONTENTS

1. INTRODUCTION.....1

2. RESEARCH OBJECTIVES.....1

3. ACCOMPLISHMENTS OF THE RESEARCH.....2

3.1 EXPERIMENTAL AND THEORETICAL ANALYSIS OF WAVE PROPAGATION IN A FLEXIBLE LATTICE STRUCTURE.....2

3.1.a Results Supplementary to Reference 1.....2

3.1.b Transient Wave Response to Suddenly Applied Cosine Force Excitation.5

3.2 DEVELOPMENT OF A FLEXIBLE SLEWING PLANE GRID LABORATORY STRUCTURE....15

3.2.a Recent Tests and Modifications.....15

3.2.b Finite Element Model and Theoretical Modal Analysis.....20

3.2.c Experimental Modal Analysis.....20

3.3 ACTIVE DAMPING AND ACTIVE CONTROL WITH STRUCTURE-BORNE SENSORS AND ACTUATORS.....22

3.3.a Reaction Wheel Control Actuators.....23

3.3.b Servo Accelerometer Control Sensors.....27

3.3.c Active Damping Experiment.....30

3.3.d The Potential for Continued Experimental Study of Active Vibration Control and Maneuvering.....33

3.3.e Author's Commentary.....35

4. PUBLICATIONS AND CONFERENCE PAPERS.....38

5. PROFESSIONAL PERSONNEL.....38

REFERENCES.....39

TABLE 1.....40

FIGURES.....41

<input checked="" type="checkbox"/>
<input type="checkbox"/>
<input type="checkbox"/>

Codes

/or

special

\* Dr. Anthony Amos is the AFOSR Program Manager.



A-1

## 1. INTRODUCTION

The general subjects of this research were the dynamics and control of flexible structures, with applications intended for future large spacecraft structures (LSS) in Earth orbit. The primary emphasis was experimental analysis of the dynamic response of small laboratory structures not intended to represent any particular LSS, but rather designed to exhibit dynamic characteristics that are generic in various degrees to LSS.

Theoretical analyses were conducted to complement directly the experimental analyses. The theoretical methods were generally state-of-the-art rather than highly innovative. The most important general objective of the research was to achieve satisfactory agreement between experiment and theory, thus validating theoretical concepts and methods for practical application or exposing the reasons why they are inapplicable or ineffective.

The work reported here was continuation of research with AFOSR sponsorship initiated in March 1982.

## 2. RESEARCH OBJECTIVES

The first objective was to conduct a detailed study of transient wave propagation in a pendulous plane grid laboratory structure; the results are presented in Section 3.1. The second objective was to complete the development and analysis of another plane grid laboratory structure, this one having a maneuverable, slewing rigid body degree of freedom; the results are presented in Section 3.2. The final objective was to apply active damping and simultaneous maneuver and vibration control to the slewing plane grid with the use of structure-borne sensors and actuators; the results are presented in Section 3.3.

### 3. ACCOMPLISHMENTS OF THE RESEARCH

#### 3.1 EXPERIMENTAL AND THEORETICAL ANALYSIS OF WAVE PROPAGATION IN A FLEXIBLE LATTICE STRUCTURE

It was proposed to study traveling waves in the VPI pendulous plane grid, Fig. 1. References 1 and 2 present representative results of major portions of the investigation. The length limits on technical articles prevented presentation in Ref. 1 of all the relevant results of interest, so additional results are presented in Section 3.1.a below. Analysis beyond that of Refs. 1 and 2 was conducted, and the results are summarized in Section 3.1.b below.

##### 3.1.a Results Supplementary to Reference 1

Suddenly applied sinusoidal (SAS), out-of-plane force excitation was imposed on joint 4 of the pendulous grid (Fig. 1) at time  $t = 0$  s. The out-of-plane flexural displacement wave produced by this excitation traveled upward and leftward from joint 4. Figure 2, for 30 Hz SAS excitation, is a series of "snapshots" of the displacement field at successive instants, with the grid drawn in oblique view. Figure 2 shows a very clean forward-moving wave for the first 0.04 s. However, beginning at about 0.04 s, the wavefront encounters the relatively stiff steel top beam. After that time, superposition of waves traveling outward from joint 4 and waves reflecting from all boundaries appears to convert the net response gradually into standing waves.

Figure 2 shows also that SAS force excitation produces comparatively large displacement at and near joint 4. This large displacement appears on Fig. 2 to be increasing monotonically, but it is actually oscillatory at a frequency much lower than the 30 Hz excitation. It is shown in Section 3.1.b that such a dominant low frequency response does not occur when the

excitation is a suddenly applied cosine, rather than sine, force. However, SAS force excitation was used throughout most of this investigation, and the dominance of the low-frequency displacement response made it desirable to measure velocity instead of displacement in the experiments. So the principal results generated in this research were graphs of relative velocity (velocity per unit force amplitude) of individual structure joints versus time after the start of excitation. Experimental measurements and corresponding theoretical calculations for SAS frequencies 15, 30, 45, 60, 90, 120, 150 and 240 Hz are shown, respectively, on Figs. 3-10.

Reference 1 notes that theoretically predicted wave speeds are generally higher than measured values. This can be observed with some difficulty from the responses at joints 1, 5, 9 and 10 for 60 Hz and higher SAS excitation (Figs. 6-10). To illustrate the observation much more clearly, the first half of the 90 Hz joint 4 experimental and theoretical responses from Fig. 7 are expanded and plotted together on Fig. 11.

The remainder of this section is a semi-qualitative discussion of factors relevant to the ability of the pendulous grid's 127-DOF finite element model to predict traveling waves. The model is described in Ref. 1; it is necessary here only to repeat that each aluminum grid member between adjacent bolted joints is represented by two beam elements of equal length, and that standard cubic polynomial displacement functions are used to represent bending of the beam elements.

The ability of a beam finite element model to represent spatially sinusoidal (or nearly so) waves, either traveling or standing, depends in part upon the ratio of wavelength to element length: the higher the ratio, the better the model will perform, in general. Consider the bending of one aluminum grid beam element into a single wavelength. The coefficients of a

cubic polynomial can be chosen such that the displacement shape is a fair approximation to one cycle of a sinusoid. However, taking three spatial derivatives of the cubic gives a constant, i.e., theoretically the shear force is constant over the entire element. This is a very poor approximation, because spatially sinusoidal (or nearly so) bending displacement should lead to spatially sinusoidal (or nearly so) shear force. For a good example, see Ref. 2.

By a similar argument, if one wavelength spans two finite elements of equal length, then the shear force over the wavelength is approximated by two piecewise constant values. Therefore, this degree of mesh refinement -- two finite elements per wavelength -- would seem to be the minimum for which the finite element model could represent waves with anywhere near reasonable accuracy. The simple beam equation relating frequency  $f$  (in Hz) to wavelength  $\lambda$  is  $f = 2\pi\sqrt{(EI/\rho A)}/\lambda^2$ . Setting  $\lambda = 610$  mm or 591 mm, the lengths of adjacent element pairs in the aluminum grid (see Fig. 1), and using the measured  $EI$  and  $\rho A$  values of the grid beams gives values of  $f$  around 75 Hz. This matches reasonably well the frequencies at which the theoretical mode count begins to deviate seriously from the measured mode count (see Ref. 1).

However, this discussion fails to explain the fair-to-good theoretical predictions of initial traveling wave responses and overall response orders of magnitude, even for SAS excitation frequencies much higher than 75 Hz (see Figs. 7-10). That modest success is probably attributable in part to the use of all 127 modes of the finite element model in the transient response calculations. The theoretical modal vectors are certainly not all

accurate, but they do constitute a complete set spanning the space of 127-element vectors. The completeness property appears to be essential to the finite element model's performance in predicting transient response.

Another important factor is the model's predicted modal density, which is very good for frequencies below about 60 Hz and fair for frequencies between 60 and 100 Hz (see Ref. 1). Modal density was not measured for frequencies above 100 Hz, but it seems likely that the model's prediction is at least a fair approximation to reality for another 100-200 Hz.

### 3.1.b Transient Wave Response to Suddenly Applied Cosine Force Excitation

The focus of all work reported in Refs. 1 and 2 is suddenly applied sine (SAS) point-force excitation. However, it has been observed recently that suddenly applied cosine (SAC) point-force excitation may well be superior for the study of traveling waves. The advantage of SAC excitation is that it does not produce dominant low frequency displacement response, as SAS excitation does. Hence, one may measure displacement directly to detect precursor and synchronous wave response, rather than having to measure velocity or acceleration. Theoretical and experimental analysis of SAC excitation is summarized in this section, and a more detailed manuscript will be submitted for publication, Ref. 3.

It is instructive first to review and expand upon the results of Ref. 2 for transient waves in a semi-infinite beam excited by suddenly applied cisoidal edge shear force excitation. Let  $\eta(\chi, \tau)$  be dimensionless beam flexural displacement, and let  $\chi$  and  $\tau$  be the dimensionless spatial coordinate and dimensionless time, respectively. Then the initial-boundary-value problem for response to suddenly applied cisoidal edge shear force excitation is

$$\eta_{\chi\chi\chi\chi} + \eta_{\tau\tau} = 0 \text{ for } \chi \geq 0, \tau \geq 0 \quad (1a)$$

$$\eta_{\chi\chi\chi} = e^{i\tau} \text{ and } \eta_{\chi\chi} = 0 \text{ for } \chi = 0, \tau \geq 0 \quad (1b)$$

$$\eta = 0 \text{ and } \eta_{\tau} = 0 \text{ for } \xi \geq 0, \tau = 0 \quad (1c)$$

Note that the real and imaginary parts of the solution are, respectively, responses to SAC and SAS excitation.

The total response solution derived in Ref. 2 is

$$\begin{aligned} \eta(\chi, \tau) = & i\sqrt{(8\tau/\pi)}\cos(\chi^2/4\tau) - i4\chi \operatorname{Re}[\alpha I(-\chi/2\sqrt{\tau})] \\ & - \alpha e^{i(\tau-\chi)} I(\sqrt{\tau-\chi}/2\sqrt{\tau}) + \alpha e^{i(\tau+\chi)} I(-\sqrt{\tau-\chi}/2\sqrt{\tau}) \\ & - \alpha e^{i(\tau-\chi)} I(\sqrt{\tau+i\chi}/2\sqrt{\tau}) + \alpha e^{i(\tau+\chi)} I(-\sqrt{\tau+i\chi}/2\sqrt{\tau}) \end{aligned} \quad (2)$$

where  $\alpha = \frac{1}{2}(1+i)$  and  $I(z) = \frac{1}{2} \operatorname{erfc}(e^{-13\pi/4}z)$ . Reference 2 focuses on the imaginary part of the solution, the response to SAS excitation, and discusses, in particular, the secular first term, which increases monotonically as the square root of time. The short-term effect of the secular term for the beam is equivalent to the dominant low-frequency displacement response to SAS excitation for the pendulous grid.

The real part of the solution, the response to SAC excitation, is contained in the last four of the six terms, and these terms are all nicely bounded for all real  $\chi \geq 0$  and  $\tau \geq 0$ . For illustration, a "snapshot" of the rightward-traveling displacement wave at  $\tau = 10$  is shown on Fig. 12.

The bounded response of the beam to SAC excitation suggests that response of the pendulous grid to SAC excitation might be free of the dominant low-frequency displacement response that occurs for SAS excitation. This is indeed the case in theory, as is illustrated by a modal solution similar to that of Ref. 1, but now for suddenly applied cisoidal excitation. The pendulous grid is represented by an N-DOF undamped, linear finite element model with matrix equation of motion

$$[m]\ddot{q} + [k]q = \underline{f} \quad (3)$$

For suddenly applied cisoidal point-force excitation with frequency  $\Omega$  at DOF  $j$ , we have

$$\underline{f}^T(t) = [0, \dots, 0, f_j(t), 0, \dots, 0] \quad (4a)$$

where

$$f_j(t) = \begin{cases} 0, & t \leq 0 \\ F_j e^{i\Omega t}, & t > 0 \end{cases} \quad (4b)$$

The structure is motionless before  $t = 0$ , so the initial conditions are

$$\underline{q}(0) = 0 \text{ and } \dot{\underline{q}}(0) = 0 \quad (5)$$

Solving this problem by standard modal analysis, we find the relative displacement of DOF  $i$  to be

$$\frac{q_i}{F_j} = \sum_{r=1}^N \frac{\phi_{ir} \phi_{jr}}{(\omega_r^2 - \Omega^2)} (e^{i\Omega t} - \cos \omega_r t - \frac{i\Omega}{\omega_r} \sin \omega_r t) \quad (6)$$

where  $\omega_r$  is the natural frequency of the  $r$ th undamped mode of vibration, and  $\phi_{ir}$  is an element of the modal matrix  $[\phi]$ , each of whose columns is orthonormalized,  $[\phi]^T [m] [\phi] = [I]$ .

As before, the real and imaginary parts of this solution represent, respectively, responses to SAC and SAS excitation. It is easy to show, in particular, that

$$(q_i)_{\text{SAC}} = \frac{1}{\Omega} (\dot{q}_i)_{\text{SAS}} \quad (7)$$

Figures 3-10 demonstrate that velocity response to SAS excitation is not dominated by low-frequency components. Therefore, displacement response to SAC excitation also should not be dominated by low-frequency components, at least in theory.

However, there is an important practical question not addressed by the theory: Is it possible to produce experimentally a close approximation to SAC point-force excitation? Most of the results of Ref. 1 suggest strongly that a good approximation to an SAS point-force can be produced by the apparatus developed in the VPI laboratory, but an SAC point-force may be

more challenging because it requires a discontinuity in the force at  $t = 0$ , as opposed to a discontinuity in the force derivative for SAS excitation.

The feasibility of practical implementation of 30 Hz SAC excitation was evaluated experimentally. With one exception, the experimental apparatus and procedure described in Ref. 1 were used. The exception was the conditioning of the excitation signal generated by the data acquisition system's digital-to-analog converter (D/A), which drives the power amplifier of the magnet-coil force actuator (Fig. 13). For the 30 Hz SAS excitation of Ref. 1, the signal was generated at a D/A rate of 512 steps per second and smoothed by a low-pass filter. However, for SAC excitation it was desirable to make the force discontinuity at  $t = 0$  as sharp as is practically possible, so the D/A rate was increased fourfold to 2048 steps per second and the smoothing filter was eliminated entirely.

Quantities measured in the experiment include the electrical current through the force actuator coil at joint 4 and displacements sensed by noncontacting proximity probes positioned near joints 4 and 9. The joint 4 coil and proximity probe are shown in Fig. 13. The proximity probe was positioned as close as possible to joint 4, but was still about 51 mm away from the joint. The force generated by the coil was nominally proportional to the current, with sensitivity of 1.33 N/A. The data signals were conditioned by instrumentation gains and Butterworth 8-pole low-pass filters, with each filter's corner frequency set at 1000 Hz, the highest possible for the data acquisition system.

The quantities measured for a relatively high excitation level are plotted on Fig. 14. The upper graph indicates that the electrical excitation was a very good approximation of a cosine applied suddenly at  $t = 0$  s. However, the lower graph shows that joint 4 responded in an unexpected

fashion, with a dominant monotonically increasing component. The positive sign of joint 4 motion corresponds physically to the actuator coil being drawn into the magnetic field assembly (i.e., toward the left on Fig. 13). The test that produced Fig. 14 was repeated with SAC excitation of the same amplitude but sign opposite to that of the upper graph of Fig. 14. Even though the polarity of excitation was changed, the coil was still drawn into the magnetic field assembly in the same monotonically increasing fashion shown on the lower graph of Fig. 14.

From Eq. 7, the joint 4 displacement response on Fig. 14 should be identical in form to the joint 4 velocity response on Fig. 4. The character of this disagreement between theory and experiment suggests the presence of some previously undetected nonlinearity. Therefore, the experiment was repeated with lower excitation levels. As expected, for progressively lower excitation the measured response was progressively closer to the theoretically predicted response. The upper two graphs of Fig. 15 show the quantities measured for the lowest excitation level consistent with maintaining a satisfactory signal-to-noise ratio. The measured displacements have been divided by the nominal excitation force amplitude to produce relative displacements comparable with the theoretically predicted quantities (from Eq. 6) shown on the lower graph of Fig. 15.

The measured response of joint 9 agrees very well with the predicted response. There is good agreement also for the initial cycle of joint 4 response, but the agreement is less satisfactory thereafter. One can identify two categories of differences between predicted and measured responses of joint 4: peak-to-peak magnitude, and positive bias of the mean value.

The peak-to-peak magnitude differences can be attributed to two factors. The first is inaccuracy in the mode shapes of the theoretical model, which probably becomes significant for times greater than about 0.1 s as the transient response changes gradually into standing wave response (for example, see Fig. 2); this is discussed in Ref. 1. The second factor is the displacement sensor's separation from joint 4 by about 51 mm. Because of this separation, response measured at the displacement sensor can be considerably different than response at joint 4. Figure 16 illustrates this point with frequency response functions of displacement measured by the displacement sensor and displacement calculated from velocity measured at joint 4.

The positive bias in the mean value of the joint 4 experimental response on Fig. 15 is more difficult to explain. However, it is clear that this bias is attributable to the same nonlinearity that produced the monotonically increasing displacement component for the higher excitation level (Fig. 14).

The probable cause of the anomalous joint 4 displacement response has been identified: The sensitivity of the force actuator varies with the depth of the coil into the magnetic field assembly. Figure 17 is a graph of calibration data measured after the observation of the nonlinear dynamic response discussed above. The actuator calibrated is not the one pictured on Fig. 13, which produced the data of Figs. 14 and 15, but the two actuators are nominally identical in design and construction. The force calibration was made with use of a PCB 208A piezoelectric force gauge. This device cannot measure static forces, so the calibration was conducted dynamically with 20 Hz sinusoidal excitation and repeated with 30 Hz

sinusoidal excitation to establish that the sensitivity is independent of frequency.

Ideally, the relative sensitivity on Fig. 17 would be unity over a wide range of depths, say  $\pm 5$  mm, about the static depth, which is labeled 0 mm. However, the sensitivity actually has a strongly parabolic variation. This characteristic is the undesirable result of the magnet-coil actuator's design. The design is based in large part on that of a conventional permanent-magnet vibration exciter (or a loudspeaker), with a cylindrical coil positioned in the annular gap between external and internal magnetic pole pieces.

However, there are two substantive differences between a conventional vibration exciter and the force actuator shown in Fig. 13: the gap width and the mechanical connection between magnetic field assembly and coil. The annular gap of a vibration exciter (or loudspeaker) is made only wide enough to barely accommodate the thickness of the coil, and the coil is attached to the magnetic field assembly by a soft spring (called a spider) which restrains the coil to translate without rotation within the gap, thus preventing the coil from scraping against the pole pieces. Making the gap as narrow as possible strongly concentrates the magnetic field within the gap. Consequently, the force/current sensitivity is almost independent of coil depth within the magnetic field assembly because the magnetic flux passes through the same number of coil windings regardless of depth.

In contrast, for the force actuator used in this study, the gap between pole pieces is relatively wide and there is no mechanical connection between coil and magnetic field assembly. These features are necessary to accommodate bending rotations of the pendulous grid to which the coil is attached, to provide some additional clearance which makes a bit easier the

difficult task of correctly mounting the coil and magnetic field assembly relative to each other, and to avoid any mechanical contact between the extremely flexible pendulous grid and the magnetic field assembly. The undesirable consequence of the wide gap between pole pieces is that the magnetic lines of flux are not concentrated, but rather stray outside of the gap. Hence, the flux passing through the coil windings varies with coil depth into the magnetic field assembly, producing the variable sensitivity shown on Fig. 17.

Theoretical transient response analysis accounting for the variable sensitivity of Fig. 17 would be a formidable task, especially for a structure as complex as the pendulous grid. It will suffice here to evaluate a greatly simplified problem which, nevertheless, includes many essential features of the actual problem. We consider a 1-DOF spring-mass system driven by SAC current excitation into a force actuator that exhibits a linearly varying force/current sensitivity. Let  $i(\tau)$  be dimensionless current excitation,  $u(\tau)$  be dimensionless displacement response,  $\tau$  be dimensionless time, and  $\beta$  be dimensionless excitation frequency. Then the equation of motion and initial conditions are

$$\ddot{u} + u = (1 + \epsilon u)i(\tau) \quad (8a)$$

$$i(\tau) = \pm \cos \beta \tau \quad (8b)$$

$$u(0) = 0 \text{ and } \dot{u}(0) = 0 \quad (8c)$$

The dimensionless parameter  $\epsilon$  is the slope of the force/current sensitivity, and it is assumed to be small so that Eqs. 8 can be solved by a simple perturbation analysis. The  $\pm$  signs in Eq. 8b allow for both polarities of excitation to be considered. Note that linearizing the force/current sensitivity simplifies differential equation 8a from being nonlinear to being linear with a varying coefficient.

We seek a solution of Eqs. 8 in the series form

$$u(\tau) = u_0(\tau) + \epsilon u_1(\tau) + O(\epsilon^2) \quad (9a)$$

This is a regular perturbation problem, for which we can find the following solution with little difficulty:

$$u_0(\tau) = \pm \frac{1}{1 - \beta^2} (\cos \beta \tau - \cos \tau) \quad (9b)$$

$$u_1(\tau) = \frac{1}{2} \frac{1}{1 - \beta^2} \left\{ [1 - \cos \tau] + \frac{1}{1 - (1 - \beta)^2} [\cos(1 - \beta)\tau - \cos \tau] \right. \\ \left. + \frac{1}{1 - (2\beta)^2} [\cos 2\beta \tau - \cos \tau] + \frac{1}{1 - (1 + \beta)^2} [\cos(1 + \beta)\tau - \cos \tau] \right\} \quad (9c)$$

Figure 18 presents numerical evaluations of excitation current, Eq. 8b (with the + sign), and response displacement, Eqs. 9. For comparison with Figs. 14 and 15, the dimensionless excitation frequency  $\beta$  is chosen to be somewhat representative of the circumstances of Figs. 14-16. The SAC excitation frequency used for the traveling wave experiment of Fig. 15 was 30 Hz, and Fig. 16 shows that the two natural frequencies of the pendulous grid closest to 30 Hz are about 29 Hz and about 30.6 Hz. Hence, the values of  $\beta$  used for Fig. 18 are  $30/29$  and  $30/30.6$ . The value of dimensionless force/current sensitivity  $\epsilon$  used is 0.2, chosen arbitrarily.

The response  $u(\tau)$  for  $\beta = 30/30.6$  on Fig. 18 has a positive bias in mean value somewhat similar to that of the joint 4 experimental response on Fig. 15. It should be noted, moreover, that the polarity of the  $O(\epsilon)$  term, Eq. 9c, is independent of the polarity of the excitation (the  $\pm$  sign of Eq. 8b). This means that the response bias for  $\beta = 30/30.6$  and  $\epsilon = 0.2$  would be positive even if the current were  $-\cos \beta \tau$ . This characteristic also matches the experimentally observed behavior described above in connection with Fig. 14.

The response  $u(\tau)$  for  $\beta = 30/29$  on Fig. 18 has a negative bias. Further analysis -- a steady-state oscillatory solution of Eqs. 8a and b assuming that small damping eventually suppresses all transients at the

natural frequency -- suggests that the sign of the bias is the same as that of the leading coefficient in Eq. 9c,  $\frac{1}{1 - \beta^2}$ ; that is, the bias is positive for excitation below resonance and negative for excitation above resonance.

Comparison of the excitation-response pairs of Fig. 18 with the experimental excitation-response pair and the theoretical response of Fig. 15 shows substantial differences as well as the similarities discussed above. For example, although the response bias of the 1-DOF case for  $\beta = 30/30.6$  has the same sign as the experimental response, the phase between excitation and response of the 1-DOF case for  $\beta = 30/29$  is much closer to the experimentally observed phase than is that of the case for  $\beta = 30/30.6$ . Furthermore, for both  $\beta$  values the 1-DOF initial responses immediately after  $\tau = 0$  are quite different than the very similar experimental and theoretical initial responses on Fig. 15. One concludes from these observations that the pendulous grid's transient response involves many modes, and that the 1-DOF model of Eqs. 8 and 9 is simply inadequate to describe the full complexity of response.

Nevertheless, the 1-DOF analysis does provide persuasive evidence that the differences between the experimental joint 4 responses of Figs. 14 and 15 and the theoretical joint 4 response on Fig. 15 are due primarily to the actuator's variable force/current sensitivity shown on Fig. 17. Therefore, if the actuator design could be modified to produce constant sensitivity without also producing mechanical stiffness or friction between the structure-borne coil and the magnetic field assembly, then a very good approximation to SAC point-force excitation could be achieved. Consequently, the advantage discussed at the beginning of this section of

SAC excitation relative to SAS excitation could be fully realized in experimental analysis of transient traveling waves.

Finally, it should be noted that the variable sensitivity of the actuator is probably the reason for a previously unexplained discrepancy between experiment and theory in the results of Section 3.1.a for SAS excitation. The discrepancy is evident in the joint 4 relative velocity responses for SAS excitation at all frequencies 60 Hz and higher, Figs. 6-10: Each measured time series exhibits a positive bias relative to the predicted time series. This positive bias in velocity corresponds directly to a monotonic positive increase in displacement such as that of Fig. 14.

### 3.2 DEVELOPMENT OF A FLEXIBLE SLEWING PLANE GRID LABORATORY STRUCTURE

It was proposed to design, build and test a rotation fixture and a flexible plane grid. The plane grid attached to the rotation fixture constitutes a flexible structure with a single, maneuverable rigid body mode. An intermediate version of this structure called the "floppy door" has been discussed extensively in Ref. 4. The final version discussed below is called the "slewing grid". This structure is illustrated in Figs. 19 and 20.

#### 3.2.a Recent Tests and Modifications

Reference 4 reported rather poor correlation between theoretically predicted and experimentally measured vibration modes of the laboratory structure. Additional testing of the structure's properties was recommended to help reconcile the theoretical model with observed dynamic behavior. The recommended tests include dynamic measurement of the rotation fixture's inertia and measurement by strain gauges of static in-plane member loads. These tests have been attempted, and the results are presented next.

The rotation fixture includes the steel shaft and steel attachment fittings labeled on Fig. 19. These members are quite stiff relative to the aluminum grid attached to them, so they are assumed rigid in the theoretical model. In fact, the fundamental bending natural frequency of the rotation fixture is in the 15-20 Hz range, which means that the mode is probably among the second ten actual structure modes. The rotation fixture's moment of inertia about the shaft axis is an important parameter for many structure modes, but the irregular geometry of the steel attachment fittings makes it a difficult quantity to calculate. Therefore, a simple dynamic measurement was attempted.

The aluminum grid was removed from the rotation fixture. Then a permanent-magnet vibration exciter was connected to the lower attachment fitting through a ball-jointed sting and a PCB 208B force gauge, and a Bently Nevada Type 300 noncontacting displacement sensor was positioned to measure motion of the lower attachment fitting. The arrangement is sketched on Fig. 21.

If no moments other than that due to the vibration exciter act on the stiff rotation fixture, then the equation governing small rotations about the shaft axis is

$$J(\ddot{x}/b) = af(t) \quad (10)$$

where  $J$  is the rotation fixture's moment of inertia to be inferred,  $f(t)$  is the force imposed by the vibration exciter,  $x(t)$  is the displacement sensor measurement, and  $a$  and  $b$  are the distances denoted on Fig. 21. For steady-state sinusoidal excitation and response, Eq. 10 can be written as an acceleration/force frequency response function,

$$\frac{-\Omega^2 X}{F} = \frac{ab}{J} \quad (11)$$

Two incremental sine sweeps were run to measure the left-hand side of Eq. (11), one sweep primarily below and the other primarily above the 15-20 Hz range of the shaft's lowest bending natural frequencies. The disappointing results are shown on Fig. 22. For both sweeps, the measured magnitude of  $-\Omega^2 X/F$ , which should be constant according to Eq. 11, varies substantially with frequency. Factors that might have contributed to the variability include: friction and/or an enigmatic stiffness of the shaft bearings (see Ref. 4, pp. 17-18); and the stiffness of the force gauge's power-signal cable. Torsional flexibility of the shaft probably was negligible since, by conservative estimate, the lowest torsion frequency of the rotation fixture is close to 200 Hz.

The magnitude on the lower graph of Fig. 22 seems to approach asymptotically a constant value of about 40 in/s<sup>2</sup> per lb (0.23 m/s<sup>2</sup> per N). Using this value to calculate J from Eq. 11 gives a rotational moment of inertia very close to one inferred previously (see Ref. 4, p. 21). Hence, the old value of J was retained in the theoretical model discussed below in Section 3.2.b.

It was demonstrated in Ref. 4 that static in-plane loads in the thin-walled aluminum grid members have a significant effect on the structure's stiffness. However, influences such as the bolt tightening process, temperature variations, and slippage in the joints may cause the calculated in-plane loads to be incorrect. Therefore, an attempt was made to measure these loads with the use of strain gauges.

It proved impossible to measure good quantitative data, in part because the necessary sophisticated instrumentation and experienced personnel were not available. A graduate student with no previous knowledge of strain gauge technology did all of the work using inexpensive instrumentation

designed for simple instructional demonstrations. Nevertheless, the testing did produce some important qualitative information.

After some initial calibration testing on beams identical to those of the aluminum grid, six strain gauges were mounted on the LH member of the disassembled grid, three near joint 2 and three near joint 5. It had been determined in the initial testing that strains associated with gravity-induced member axial tension or compression were beneath the resolution of the instrumentation. In-plane bending moments were within the resolution, but the moment induced by gravity could not be measured because the complex process of assembling the slewing grid (see Ref. 4, p. 15) required that all instrumentation be disconnected during assembly. So the only measurable quantity was the in-plane bending moment generated by tightening the bolts.

Bolts at the five joints were hand-tightened several different times in different orders, and the final moments produced at the two stations along the LH member were recorded each time. The final moments varied substantially with the tightening sequence and, in every case, were of the same order of magnitude as the predicted gravity-induced moments. The geometric stiffness matrix of the theoretical model is based on the predicted in-plane gravity loads. Unfortunately, the strain gauge measurements suggest that the actual loads may be very different than predicted due to the bolt tightening process.

After the strain gauge measurements were completed, the LH member on which strain gauges were mounted was removed and stored for possible later use. It was replaced for the dynamic testing by a beam member without strain gauges but identical in all other respects. This was desirable both to protect the strain gauge installation and wiring, and to minimize the quantity of electrical wire carried by the dynamic test specimen.

Several other modifications have been made to the slewing plane grid relative to the configuration reported in Ref. 4. There was evidence that the shaft was not well aligned with gravity (Ref. 4, p. 16). Hence, the shaft mounting bolts were loosened and the shaft was re-aligned as carefully as possible with the use of a borrowed bubble inclinometer. The only detectable difference resulting from this effort was a change in the stable static angular position of the entire slewing grid, so it is doubtful that any real progress was made.

To prevent the recurrence of a previous problem (Ref. 4, p. 19), nonmagnetic 316 stainless steel nuts, bolts and washers were used at joints 3, 4 and 5. To expedite installation of control hardware, the bolts for all joints were machined as follows: A hole was drilled axially through the bolt to accommodate a long 10-32 screw; also, the bolt head was machined flat to permit uniform contact with the flat base of a reaction wheel frame or an accelerometer mounting adapter.

Before the control and excitation hardware devices shown in Fig. 20 were mounted on the structure, the inertia properties were carefully measured for use in the theoretical model. For example, the reaction wheel and accelerometer of joint 3 were bolted together just as shown in Fig. 23 (including spacers representing the aluminum beams), but separate from the structure. Then the weight and center of gravity of the assembly were measured. Finally, the moments of inertia of the assembly about both horizontal and vertical centroidal axes were measured in tedious bifilar pendulum tests.

The arrangement of control and excitation hardware on the structure was designed to preserve as much as possible the ideal characteristics represented by the theoretical model. To minimize static tilting and

twisting of the grid due to the relatively large center-of-gravity offsets of the reaction wheels, the reaction wheels were mounted in a somewhat balanced fashion, with offsets to the left at joints 3 and 4 and to the right at joint 5, as shown on Fig. 20. Also, the lightest electrical wires available were used, and all wires for the control hardware (reaction wheels and accelerometers) were routed loosely off the structure near joints 1 and 2, as shown on Fig. 24, thus minimizing the addition of stiffness against rigid body rotation of the structure.

### 3.2.b Finite Element Model and Theoretical Modal Analysis

The final 49-DOF finite element model is identical in form to the model described previously (Ref. 4, p. 21). Of course, appropriate parameter values were updated to reflect the modified hardware, particularly weight and inertia values for control hardware bolted to the five joints. However, no attempt was made to model the influence on the slewing grid's dynamics of the electrical wires connected to the control and excitation devices.

In-plane loads were expected to have significant influence on overall structure out-of-plane stiffness. Accordingly, the geometric stiffness matrix was calculated on the basis of predicted in-plane loads resulting from the structure's own weight. No attempt was made to account for changes in the loads that tightening the bolts might have produced. It is relevant that the predicted dead-load compression in the critical LH member exceeds the pin-ended Euler buckling compression by 14%.

The theoretical natural frequencies and mode shapes for the eight modes with frequencies under 10 Hz are shown on Figs. 25a and b.

### 3.2.c Experimental Modal Analysis

Frequency response functions (FRF) of the slewing grid were measured, with force excitation provided by coils attached to the DWD and LH members,

and with accelerations sensed at the bolted joints; see Fig. 20. For each FRF, single-point random excitation was imposed. Fast Fourier transforms of the excitation and response signals were calculated, and the data from four distinct, consecutive sample periods was averaged to produce baseband FRFs with frequency resolution of 0.04 Hz. No artificial data windowing was used. A theoretical modal model was fit to the averaged data. The modal parameters inferred from this process are listed on Table 1. Also listed for comparison are the theoretical natural frequencies from Figs. 25a and b.

The nonzero natural frequency of the fundamental mode is the consequence of a small nonlinear stiffness of unknown origin (Ref. 4, pp. 17-18, 21), to which the electrical wires might contribute (see Fig. 24). This stiffness does not prevent slewing of the structure through small angles, but it does complicate the maneuver. An artificial rotation stiffness is added to the shaft rotation DOF in the finite element model to approximate the observed behavior.

The quality of agreement on Table 1 between measured and predicted modes is good for all except modes 4 and 7. However, the difference between measured and predicted natural frequencies of modes 4 and 7, especially the former, is very disappointing and evidently indicates a serious shortcoming of the theoretical model.

The slewing grid is, with one exception, a fairly simple structure. The exception is the effect on the structure's stiffness of the in-plane static loads in the thin-walled beam members caused by the structure's own weight, by tightening of the joint bolts, and by temperature changes. The predicted deadweight loads have been used in the geometric stiffness matrix of Argyris et al. (Ref. 5). In particular, the geometric stiffness matrix substantially reduces the total stiffness of the LH member, which is

predicted to be heavily compressed. The LH member is indeed heavily compressed, as evidenced by leftward static bowing of as much as 1-2 thicknesses at its midpoint (Ref. 4, pp. 20 and 30).

However, manual static flexing of the compressed LH member and of the structurally identical but uncompressed UH member fails to confirm, at least qualitatively, the prediction of reduced stiffness in the LH member. This observation suggests that the geometric stiffness matrix of Ref. 5 has been applied inappropriately to a situation which requires a more accurate large-displacement theory. It is clear from the shape of mode 4 on Fig. 25a that stiffening of the LH member in the theoretical model would raise the natural frequency of mode 4 toward the measured value in Table 1.

### 3.3 ACTIVE DAMPING AND ACTIVE CONTROL WITH STRUCTURE-BORNE SENSORS AND ACTUATORS

It was proposed to conduct flexible-structure control experiments with the use of structure-borne control hardware consisting of linear servo accelerometers as sensors and reaction wheels as actuators. The experiments originally planned were active vibration damping on both the pendulous grid (Fig. 1) and the slewing grid (Fig. 19), and simultaneous maneuvering and vibration damping on the slewing grid. After the original proposal, it was decided to conduct control experiments only on the slewing grid because the pendulous grid was tied up by the traveling wave experiment (Section 3.1) and because installing the hardware first on the pendulous grid and later on the slewing grid would be a duplication of effort not justified by the potential benefits.

### 3.3.a Reaction Wheel Control Actuators

Five nominally identical small reaction wheel actuators were built, tested extensively, and then mounted on the slewing grid, as shown on Figs. 20, 23, 24 and 26. The designs of both the mechanical actuator and the controlled-current power amplifier driving the actuator were based on designs developed by Montgomery and associates at NASA Langley Research Center, Ref. 6. The heart of the actuator is a Model QT-0714-B torque motor manufactured by Inland Motor Division of Kollmorgen Corp., with maximum torque rating of 20 oz-in (0.14 N-m).

Building, testing and using the reaction wheel actuators has been a difficult and time-consuming experience, primarily because of a single, serious flaw in the design: the coupling between the torque motor shaft and the flywheel shaft. This coupling is referred to as a "poor man's universal joint", and it is intended to prevent bending of the motor shaft caused by unavoidable slight misalignment between the motor shaft and the much stiffer flywheel shaft.

The coupling is produced as follows (see Fig. 27). A small hole is drilled diametrically through the motor shaft near the shaft's outside end, and a slightly oversized steel pin of several shaft diameters length is pushed into the hole until equal lengths protrude out of each side of the motor shaft. A hole bigger than the motor shaft is drilled axially into the end of the flywheel shaft that couples with the motor shaft, and a slot of width equal to the pin diameter is machined diametrically into the same end. Thus, the motor shaft and its pin fit into the flywheel shaft and its slot and, ideally, a perfect coupling is effected by contact between the two ends of the pin and the sides of the slot in the flywheel shaft. The flywheel shaft is machined from brass, so that the natural lubricating property of

brass expedites axial sliding on the surfaces of contact to compensate for misalignment between the two shafts.

Unfortunately, the actual hardware rarely functions ideally. It is difficult to achieve a good match between pin diameter and diameter of the hole through the motor shaft. Hence, when the wheel spins or oscillates, the pin has a tendency to work its way out of the shaft. In fact, in Fig. 26 the end of the pin is protruding outside the slot in the flywheel shaft; it had worked out of the shaft until it contacted the inside surface of the mating block between motor and flywheel, causing the actuator to bind.

It is also difficult to achieve a good match between the pin diameter and the width of the slot in the flywheel shaft. If the slot width is less than the pin diameter, then the pin will not fit into the slot. Consequently, the slot width must inevitably be slightly greater than the pin diameter, and this leads to backlash in the coupling. Furthermore, the backlash increases as the actuator is tested or used in an oscillatory fashion because the hard steel pin plastically dents the soft brass flywheel shaft at the contact surfaces.

Figures 28-31 are copies of a digital oscilloscope screen showing examples of torque generated by two of the actuators in response to sinusoidal voltage inputs to their power amplifiers. The torques were measured on a testing apparatus of the type devised for calibrating the original NASA Langley actuators (Ref. 7): An actuator was fastened to the center of a rigid bar and each end of the bar was attached to a mechanically grounded force gauge; the dynamic force signals were multiplied by the common moment arm, then one was subtracted from the other, thus producing a signal proportional to the moment generated by the actuator.

The torque signal shown on Fig. 28 is almost perfect; only a hint of backlash appears near the peaks. However, with no change other than a 90° rotation of the flywheel position, the severe backlash evident on Fig. 29 occurred; the actuator clattered loudly during this test. The dependence of backlash on flywheel position is due to misalignment of the motor and flywheel shafts. At lower driving frequencies, the severity of the backlash decreased, as shown on Fig. 30.

The torque generated by this actuator design can be contaminated also by ripple due to commutation in the motor and by noise from the bearings, two each supporting the motor shaft and the flywheel shaft. Bearing noise is especially evident when an actuator is operated with an angular velocity bias, as shown on Fig. 31.

The manufacturer's published average sensitivity of the QT-0714-B torque motor is  $K = 4.02 \text{ oz-in/amp}$  ( $0.0284 \text{ N-m/amp}$ ). In combination with the power amplifier's sensitivity of  $0.500 \text{ amp/volt}$ , this gives a nominal output torque/input voltage sensitivity of  $0.126 \text{ lb-in/volt}$  ( $0.0142 \text{ N-m/volt}$ ). Also, the manufacturer provided an individual static calibration with each motor. Nevertheless, it seemed prudent to perform a dynamic functional check and calibration on each combination of reaction wheel and power amplifier before using the actuators in active control experiments. This dynamic testing revealed some assembly defects in both reaction wheels and power amplifiers (which were then fixed), and it provided further insight into the shaft-coupling design flaw described above.

The testing consisted of an incremental sine sweep on each actuator to measure an output torque/input voltage frequency response function. Each sweep was from 2 to 20 Hz in increments of 0.2 Hz, with a minimum of 10

cycles delay between data points. Output torque was measured with the use of the dual-force calibration apparatus described above (Ref. 7).

Figure 32 shows typical FRFs measured from one actuator for two different levels of excitation. The FRF magnitudes are neither constant nor smooth, and the differences between the two cases seem indicative more of erratic response than of nonlinearity. The mean flywheel position cannot be controlled, so the erratic response was probably due to somewhat randomly varying positions during the sweeps, leading to similarly varying levels of backlash (cf. Figs. 28 and 29). Moreover, it appears likely that the digital filter in the sine-testing software was unable to remove completely the backlash noise.

Similarly erratic FRFs were measured in sine sweeps on the other actuators. However, most of the magnitude data, though varying with frequency, lies within the range 0.12-0.13 lb-in/volt. In view of this small range of variability, it was decided to use the nominal sensitivity of 0.126 lb-in/volt (0.0142 N-m/volt) from the manufacturer's specifications for all of the actuators in subsequent applications. This should suffice for all practical purposes.

For the possible application of maneuvering the slewing grid laboratory structure, it was desirable to determine, at least qualitatively, the torque-speed characteristics of the reaction wheel actuators. The equation of motion assumed to apply is

$$J \dot{\omega} + C\omega + F \operatorname{sgn}(\omega) = Ki \quad (12)$$

where  $\omega(t)$  is the angular velocity of the flywheel,  $i(t)$  is the current driving the motor,  $J$  is the polar moment of inertia of the flywheel and the coupled rotating portion of the motor,  $C$  is the viscous damping constant,  $F$  is the dynamic Coulomb friction, and  $K$  is the motor's

sensitivity. For constant current  $I$ , the steady-state output speed from Eq. 12 is

$$\Omega = -\frac{F}{C} - \frac{K}{C} I \quad (13)$$

The objectives of this test were to determine the validity of Eq. 13 for the reaction wheel actuators and, if it is valid, to measure the damping constants  $C$  and  $F$ .

With the use of a strobotac, measurements were made of steady-state speed versus current on actuator #1. It was determined that, for current under about 0.5 amp, the data fit the linear model Eq. 13 reasonably well. With the parameters calculated from a linear least-squares curve fit and with the manufacturer's value for  $K$  given above, the damping constants calculated are

$$C = 2.8E-3 \text{ oz-in/rad/s (2.0E-5 N-m/rad/s)}$$

$$F = 0.32 \text{ oz-in (2.3E-3 N-m)}$$

These data were measured on only one actuator, so they may not apply to any of the others. The damping values are obviously very dependent on the quality of the bearings used to support the flywheel, on how the bearings are seated in the frame, and on how the flywheel shaft is seated in the bearings. The uniformity of all these factors from one actuator to the next is uncertain.

If one attempts to increase the constant input current above about 0.5 amp, the back emf of the motor overpowers the current control capability of the power amplifier. Hence the motor speed is limited. For actuator #1, the speed limit is about 6,000 rpm.

### 3.3.b Servo Accelerometer Control Sensors

Five QA-900 linear servo accelerometers were purchased from Sundstrand Data Control, Inc. Special mounting adapters were fabricated, and the

accelerometers were mounted on the slewing grid as shown on Figs. 20, 23, 24 and 33. Servo accelerometers are used in control applications, rather than the more common and less expensive piezoelectric accelerometers, because their bandwidth extends down to 0 Hz and their adjustable sensitivity can be set to generate strong signals for even low-amplitude motion at low frequencies. Disadvantages of servo accelerometers include relatively high cost and fragility, which necessitates very careful handling.

There are additional disadvantages associated with the use of linear accelerometers for control experiments on the slewing grid. For active damping, the most effective type of sensor to use in conjunction with a reaction wheel torque actuator is a colocated angular velocity sensor. Producing a facsimile of such a device with linear accelerometers requires, in general, an accelerometer pair mounted on a rigid bar (called a dual linear accelerometer arrangement) and integration of the acceleration signals.

Figure 33 shows the one true dual linear accelerometer arrangement used on the slewing grid. The sensor pair combined with the reaction wheel actuator at joint 5 constitutes a colocated sensor-actuator arrangement for frequencies well below the fundamental frequency of the center-supported beam with end-mounted accelerometers.

Figure 24 shows the other arrangement used on the slewing grid to measure angular acceleration. Provided that the rotation fixture (attachment fittings and steel shaft, see Fig. 19) remains effectively rigid, the output of the accelerometer at joint 2 is proportional to the angular acceleration of the rotation fixture. Furthermore, the accelerometer at joint 2 combined with the reaction wheels at both joints 1

and 2 constitutes a colocated sensor-actuator arrangement for frequencies well below the lowest bending natural frequencies of the rotation fixture.

Integration of the acceleration signals to produce velocity signals has presented difficulties. One option was to use the precision analog integrators of an available analog computer. However, this option would require the powering and insertion into the control loop of an additional instrument, the analog computer. But it is desirable to minimize the number of instruments in the control loop, for experience has shown that instabilities and/or erratic behavior due to electrical aberrations generally result from the use of too many instruments. Hence, it was decided not to use analog integration, but rather to integrate digitally on the PC-1000 digital controller, Fig. 34, which would be in the control loop in any event to accept sensor signals and generate actuator commands.

The first type of digital integration tried on the PC-1000 was direct solution of

$$\dot{x} = y \quad (14)$$

where  $x$  is the velocity signal and  $y$  is the acceleration signal.

Discrete-time solution of Eq. 14 gives

$$x(k + 1) = x(k) + \Delta t y(k) \quad (15)$$

where  $\Delta t$  is the sampling period and the integer within parentheses denotes the time instant. Equation 15 implemented on the PC-1000 is statically unstable; the output diverges slowly until the instrument overloads.

A simple approximation to Eq. 14 is

$$\dot{x} + ax = y \quad (16)$$

Constant  $a$  can be chosen such that the error in the solution of Eq. 16 relative to that of Eq. 15 is less than a specified quantity for all frequencies above a lower limit. For a sample period of 0.0005 s, the

discrete-time solution of Eq. 16 which produces less than  $10^\circ$  phase error for all frequencies above 0.5 Hz is

$$x(k + 1) = 0.9997382 x(k) + 0.0004999346 y(k) \quad (17)$$

Equation 17 implemented on the PC-1000 is statically stable (which is amazing in view of how slight is the difference between Eq. 17 and Eq. 15), and it integrates accurately for frequencies above 0.5 Hz. Signals with frequency content below 0.5 Hz are not integrated but rather are low-pass filtered with gain  $1/a$ . Hence, a control loop arranged to feed back negative velocity is really feeding back something closer to negative acceleration for the sensor signals below 0.5 Hz, thus actively increasing inertia rather than damping.

### 3.3.c Active Damping Experiment

An experiment was conducted to apply direct, uncoupled, velocity feedback active damping to the slewing grid using the colocated sensor-actuator combinations on the rotation fixture (joints 1 and 2) and at joint 5. The feedback equation implemented is

$$T = -C\dot{\theta} \quad (18)$$

where  $T$  is torque generated by reaction wheel actuators,  $\dot{\theta}$  is angular velocity calculated from acceleration signals, and  $C$  is the active damping constant.  $C$  was chosen, somewhat arbitrarily, to be  $14 \text{ lb-in/rad/s}$  ( $1.6 \text{ N-m/rad/s}$ ) for joint 5 and twice that value for the rotation fixture.

The PC-1000 digital controller, Fig. 34, executed Eqs. 17 and 18. It was operated at its maximum rate,  $1/\Delta t = 2,000 \text{ steps/s}$ , to minimize the effect of discrete-time operation, especially the computational delay of  $1.35 \Delta t$  (Ref. 8).

Passive, single-pole RC filters were used to condition the control signals. The output of each accelerometer was low-pass filtered with

nominal filter corner frequency of 477 Hz to remove high frequency noise from the signals entering the digital controller. Each command signal from the digital controller was effectively band-pass filtered between controller and power amplifier, with nominal high-pass corner frequency of 0.032 Hz and nominal low-pass corner frequency of 251 Hz. The high-pass stage was intended to remove DC signals (due, probably, to the approximate integration Eqs. 16 and 17) so that the actuator would not spin with an angular velocity bias; and the low-pass stage smoothed the stairstep form of the command signals generated by the controller's digital-to-analog converter.

Unwanted DC offset voltage generated by the PC-1000 digital controller caused difficulty. The DC offset originated at the analog-to-digital converter (A/D) at the instrument's front end, which could not be balanced to produce zero offset. The A/D offsets on most channels were 20-30 mV. That order of offset by itself is not large, but when multiplied by a feedback gain on the order of 100, the small front-end offset becomes a huge output offset, which can contribute to overloading an output channel and destabilizing the control system. Hence, it was desirable to nullify, or at least minimize, the controller A/D offsets. This was done with the use of a feature of the servo accelerometers that allows the user to superimpose onto the acceleration signal a DC offset equal but opposite to the associated A/D offset.

When the simple active damping of Eq. 18 was first tried, positive damping of low-frequency motion was visually obvious, but then a high-frequency vibration appeared and gradually increased in magnitude until instruments began to overload. Contrary to all expectations, the control system supposedly consisting of only colocated sensor-actuator combinations was unstable. Investigation revealed that the instability was in an 18.4 Hz

side bending mode of the rotation fixture. Thus, because of the steel shaft's flexibility, the accelerometer and the reaction wheel actuator at joint 2 were, in fact, not effectively colocated.

It is a bit difficult to see how the reaction wheels at joints 1 and 2, which exert torques about a vertical axis, were able to excite side bending of the shaft. However, the center of mass of the entire rigid assembly consisting of attachment fitting, actuator and accelerometer is considerably offset from the shaft axis (see Fig. 24). This mass eccentricity probably is the factor responsible for the rotation-bending coupling that permitted the actuators to excite side bending.

To eliminate the unstable shaft side bending, a small air dashpot manufactured by the Airpot Corporation was installed between the center of the steel shaft and the left-hand flange of the channel section connecting the entire structure to the laboratory wall (see Fig. 20). Both ends of the dashpot's piston rod are ball-jointed, so the dashpot does not restrain small rotation of the steel shaft. For excitation applied directly onto the aluminum grid, as by the force actuators on the DWD and LH members, the dashpot provided enough restraint to prevent side-bending instability. However, if the shaft itself was excited above a low threshold level, then the side-bending instability would again appear despite the damping provided by the dashpot. Hence, care was exercised to prevent any direct excitation of the steel shaft whenever the control system was turned on.

The measured performance of the active damping system applied to the slewing grid is shown on Fig. 35, which consists of open- and closed-loop acceleration/force FRFs in the 0-10 Hz range. The experimental procedure for measuring the FRFs is described in Section 3.2.c. The open-loop FRFs show evidence of all eight modes listed on Table 1. The closed-loop FRFs

demonstrate that the active damping system substantially attenuated response in modes 3-7. Moreover, it appears to have eliminated mode 7 entirely or, perhaps, to have forced modes 7 and 8 to merge into a single, heavily damped mode.

#### 3.3.d The Potential for Continued Experimental Study of Active Vibration Control and Maneuvering

Several more advanced control experiments were proposed for this research. Unfortunately, so many unforeseen obstacles were encountered in accomplishing the tasks described above and in Ref. 4 that no time remained to complete all of the proposed tasks. However, considerable preparation was made and even some preliminary testing was done in anticipation of the advanced experiments. That preparatory work, which is the basis for continued experimental study, is summarized in this section.

It was proposed to apply methods of modern control theory in addition to the simpler velocity feedback method discussed in the previous section. Therefore, state-of-the-art control design software was needed. The commercially available options included relatively expensive programs to be run on a remote mainframe computer and much less costly programs to be run on a local personal computer (PC). The PC programs generally provide all of the mathematical functions and algorithms of the mainframe programs, but can solve only problems with many fewer DOFs (state variables) than can the mainframe programs. The advantages of low cost and local authority were considered more important than the capability for solving very large problems, so the option of PC control design programs was selected.

The first program purchased was MATRIXx/PC, developed and sold by Integrated Systems Inc. To run this program and take full advantage of its graphics capabilities, it was necessary to upgrade the configuration of an

IBM-PC AT already in the laboratory and to purchase a digital plotter. Unfortunately, the maximum problem size that MATRIXx/PC proved able to solve is smaller even than had been anticipated. Therefore, another program was purchased that can solve larger problems on a PC, PC-MATLAB, developed and sold by The MathWorks Inc. The capabilities of PC-MATLAB have proven quite satisfactory in applications to date.

A computer program called MAPMODES developed by the author was used to calculate the 49-DOF finite element model and the theoretical modes of the slewing grid. Prior to the acquisition of PC-MATLAB, MAPMODES was run only on the mainframe computer. To employ the considerable PC power available, a version of the program called PC-MAPMODES was written to run on PCs; and to expedite the transfer of structural model data into PC-MATLAB, appropriate output capabilities were added to PC-MAPMODES.

The combination of PC-MAPMODES and PC-MATLAB was used to prepare a design based on modern control theory for active vibration control of the slewing grid. The design included linear-quadratic-Gaussian control of a reduced-order structural model and state estimation from accelerometer data. This design was not implemented experimentally because the structural model failed so badly to predict the actual modes of the slewing grid (Table 1). However, a similar design developed with this software was implemented very successfully in another research study, Ref. 8. Therefore, the potential clearly exists for applying modern control methods to the slewing grid, pending only a satisfactory solution of the structural modeling problem.

The capability of the reaction wheel actuators for rigid body maneuvering of the slewing grid was tested qualitatively. Actuators were mounted at joints 3 and 5 with their flywheel axes oriented vertically. A step voltage input was applied to the power amplifiers of both actuators,

and the flywheels spun up. In response, the structure slewed through an angle of, perhaps, 10-15° until the flywheel speeds reached their steady-state limits and the structure came to rest (except for vibrations induced by the spinning flywheels). Then the input voltage was removed suddenly from the power amplifiers. As the flywheels spun down, the structure slewed in the opposite direction, coming to rest at approximately the original position just as the flywheels stopped spinning.

This visually observed behavior agrees qualitatively with theoretical prediction based on the actuator model Eq. 12. Therefore, it should be possible in the future to superimpose vibration control signals upon maneuvering command signals into the power amplifiers and, hence, to produce simultaneous maneuvering and vibration control moments with the reaction wheel actuators.

### 3.3.e Author's Commentary

Much less has been accomplished than was proposed for this experimental study of active control with structure-borne sensors and actuators. The deficiency is not due to an insufficient quantity or quality of effort devoted to the project or even to an unreasonable expectation at the proposal stage of what could be achieved. Rather, the project seems to have fallen victim to Murphy's Law at almost every turn.

The most serious problem, which is still not solved, is that the finite element model of the slewing grid failed to predict satisfactorily the actual dynamic behavior. The author spared no effort to refine the model, but to no avail. The problem was quite unexpected. When proposed, the slewing grid concept seemed to be similar to but simpler than the previously developed pendulous grid. The author and his graduate students had produced an extraordinarily accurate finite element model of the pendulous grid, Ref.

1, and it seemed very likely that a comparably accurate model of the structurally simpler slewing grid should be easy to develop.

The second serious but unforeseen problem was the mediocre performance of the reaction wheel actuators. The design was developed and applied first at NASA Langley Research Center, and the author and a graduate student had even used some of the NASA-built actuators in an experiment (Ref. 7). These early experiences gave no hint of the mechanical coupling design flaw and its consequences that appeared later in the fabrication, testing and application of the actuators built for this project.

The third serious problem was the failure in many respects of the PC-1000 digital controller to perform as it should have. The PC-1000, developed and sold by Systolic Systems Inc. of San Jose CA, is perhaps the only relatively inexpensive instrument available on the market with which a researcher can easily implement both classical and modern linear control techniques on moderately sized problems and at high speed. The author and his graduate students had used the PC-1000 previously in studies of output feedback control (e.g., Ref. 9) with relatively little difficulty. There was no reason to suspect that the instrument might fail to function properly in the tasks proposed for this project. However, when we began to implement more advanced control techniques, serious problems appeared in both the hardware and software of the PC-1000. For example, at one time the PC-1000 would not accept any control design that occupied more than about one-quarter of its capacity (a software problem), and it would not execute at the rated speed of 2,000 steps/s any moderately sized control design involving a state estimator (a hardware problem).

Coping with the PC-1000 problems cost us great quantities of time and energy spent in troubleshooting and documenting the problems, communicating

with Systolic Systems, and sending the delicate instrument back and forth between Virginia and California. At this writing, many but not all of our PC-1000's malfunctions have been repaired. Equally important, we understand much better than before its idiosyncrasies and practical operating limits. Moreover, by demonstrating design deficiencies, we have helped Systolic Systems to improve the PC-1000's functioning and reliability. Finally, the author is in contact with several other researchers who have purchased a PC-1000, or will do so, and this communication will undoubtedly help them to avoid the frustrating and time-consuming problems that we have experienced.

The final serious problem, which certainly was predictable, is the general difficulty of doing experimental research in control-structural dynamics interactions. The author is convinced that effective and efficient research in this area requires both excellent laboratory facilities and the timely services of highly competent laboratory technicians and machinists and of experts in structural dynamics and control theory, laboratory instrumentation, circuit design, and machine design. We do have some of the finest laboratory instrumentation available, but our laboratory space itself is an open, public thoroughfare that is environmentally uncontrolled and exposed to noise, building vibration, and even air pollution from surrounding wind tunnels and large motors. The services of an electronics technician and a machinist are available on request, but they often cannot react in a timely fashion due to other jobs ahead of ours in the queue. Finally, the author and his graduate students attempt to fill the roles of all the technical experts, but the breadth and depth of our knowledge and experience falls considerably short of expertise.

#### 4. PUBLICATIONS AND CONFERENCE PAPERS

Reference 1 was presented at a conference and published in the proceedings, and it has been accepted for publication in a journal. Reference 2 was published in a journal. Reference 3 will be submitted for publication in a journal.

#### 5. PROFESSIONAL PERSONNEL

Principal Investigator: William Hallauer

Graduate Research Assistants:

Dinesh Trivedi: M.S. degree received June 1987

George Schamel: Ph.D. candidate

Scott Messer: M.S. candidate

## REFERENCES

1. Hallauer, W.L. Jr. and Trivedi, D.J., "An Experimental Study of Transient Waves in a Plane Grid Structure," AIAA Paper 87-0943 in AIAA CP873 Part 2B, AIAA Dynamics Specialists Conference, April 1987, pp. 888-899. Accepted for publication in AIAA Journal, tentatively scheduled for the Dec. 1987 edition.
2. Hallauer, W.L. Jr., "Transient Waves in a Beam Excited by Sinusoidal Edge Shear Force," Journal of Applied Mechanics, Vol. 54, June 1987, pp. 468-470.
3. Hallauer, W.L. Jr., "Transient Wave Response to a Suddenly Applied Oscillatory Point Force," manuscript to be submitted to Experimental Mechanics.
4. Hallauer, W.L. Jr. and Kubis, A.J. Jr., "Experimental Study of Active Vibration Control," Annual Technical Report to the AFOSR for Contract F49620-85-C-0024, July 1986, pp. 7-33.
5. Argyris, J.H., Hilpert, O., Malejannakis, G.A. and Scharpf, D.W., "On the Geometrical Stiffness of a Beam in Space--A Consistent V.W. Approach," Computer Methods in Applied Mechanics and Engineering, Vol. 20, 1979, pp. 105-131.
6. Montgomery, R.C., "Experiments in Structural Dynamics and Control Using a Grid," Workshop on Identification and Control of Flexible Space Structures, San Diego CA, June 1984.
7. Russillo, C.M., "A Study of Actuator Reconfiguration and Related Implementation Issues in Active Vibration Damping," M.S. thesis, VPI&SU, May 1985.
8. Martinovic, Z.N., Schamel, G.C. II, Haftka, R.T. and Hallauer, W.L. Jr., "An Analytical and Experimental Investigation of Output Feedback vs. Linear Quadratic Regulator," AIAA Paper 87-2390 in AIAA CP878 Vol. 1, AIAA Guidance, Navigation, and Control Conference, August 1987, pp. 628-638.
9. Skidmore, G.R. and Hallauer, W.L. Jr., "Experimental-Theoretical Study of Active Damping with Dual Sensors and Actuators," AIAA Paper 85-1921 in AIAA CP856, AIAA Guidance, Navigation, and Control Conference, August 1985, pp. 433-442.

Table 1 Experimental and theoretical modes of the slewing grid in the 0-10 Hz range

Mode $r$	Theoretical		Experimental	
	$f_r$ (Hz)	$f_r$ (Hz)	$\zeta_r$	Mode Shape Description *
1	0.20	0.29	0.05	Nearly rigid body rotation
2	0.81	0.86	0.004	Global twisting
3	2.27	2.43	0.01	Global bending
4	3.61	4.48	0.01	Bending of LH and V members out-of-phase with each other
5	4.93	5.10	0.004	
6	5.67	5.74	0.008	
7	8.12	9.43	0.004	
8	9.70	9.77	0.01	

\* Mode shapes were observed only visually and by the five accelerometers mounted at the bolted joints (Fig. 20). These observations sufficed to show that the shapes of measured modes 1-4 agreed at least qualitatively with their theoretically predicted counterparts (Fig. 25a). However, the remaining modes were dominated by higher frequency motion between the bolted joints (see Figs. 25a, b), so it was not possible to measure the mode shapes with the available means of observation.



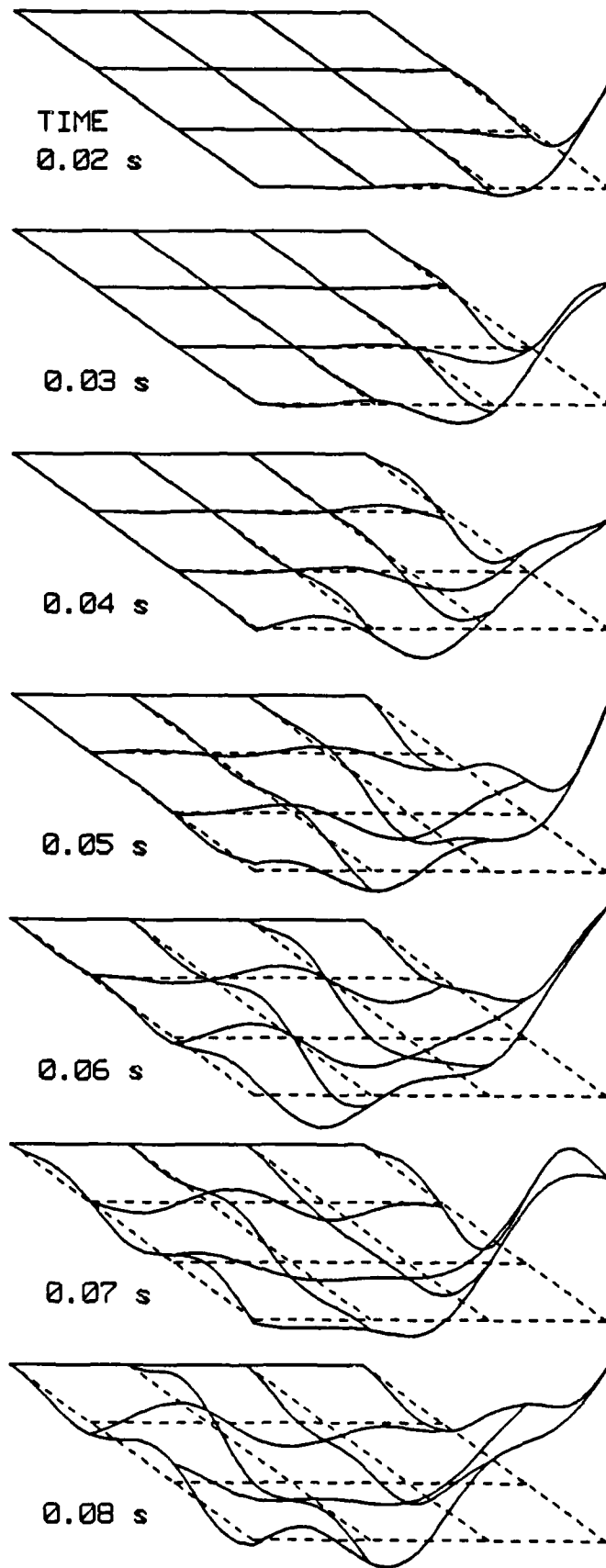


Fig. 2 Theoretical solution for displacement response (with magnitude greatly exaggerated) to 30 Hz SAS force excitation at joint 4.

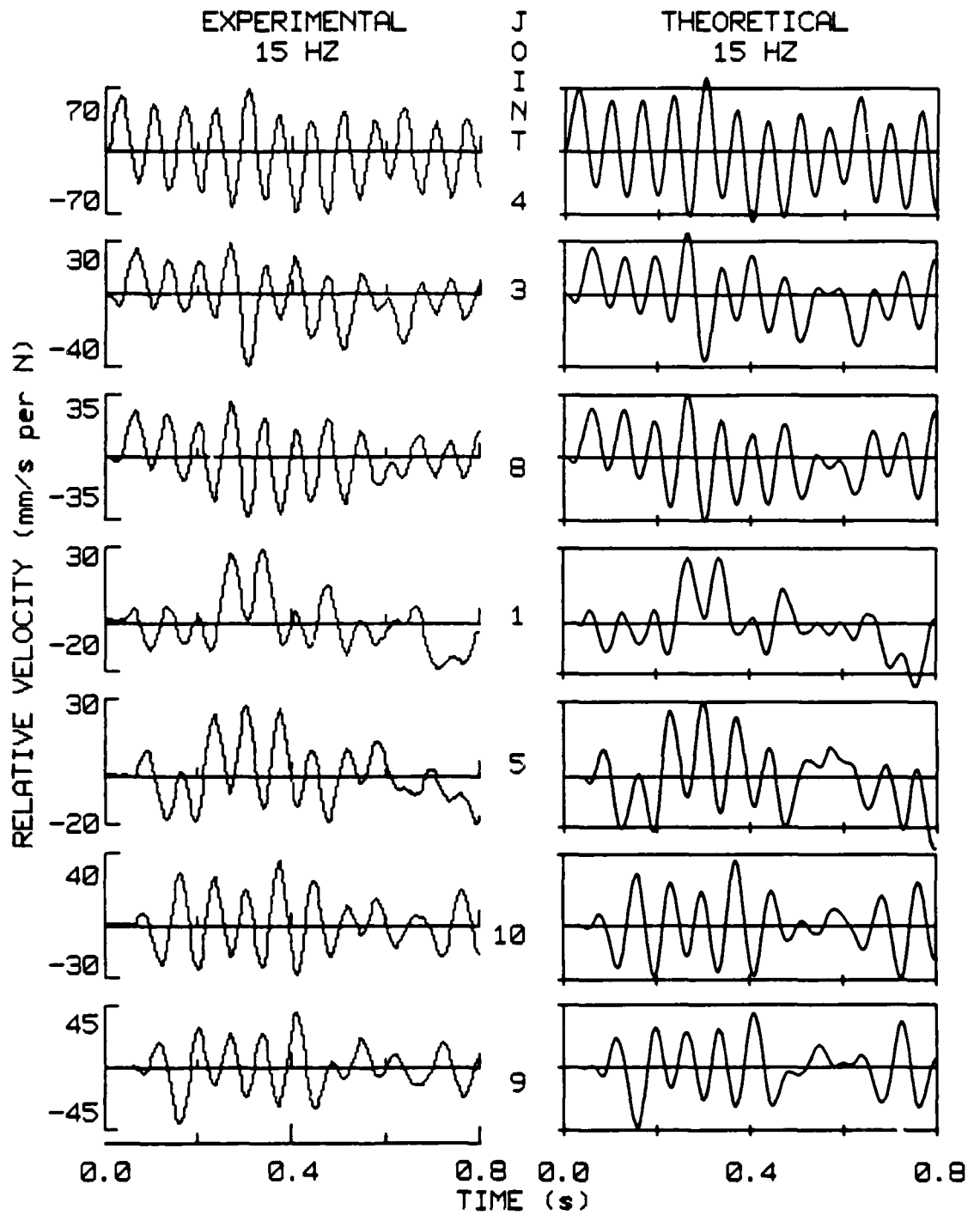


Fig. 3 Response to 15 Hz SAS force at joint 4 beginning at  $t = 0$  s. The nominal force amplitude was 0.201 N.

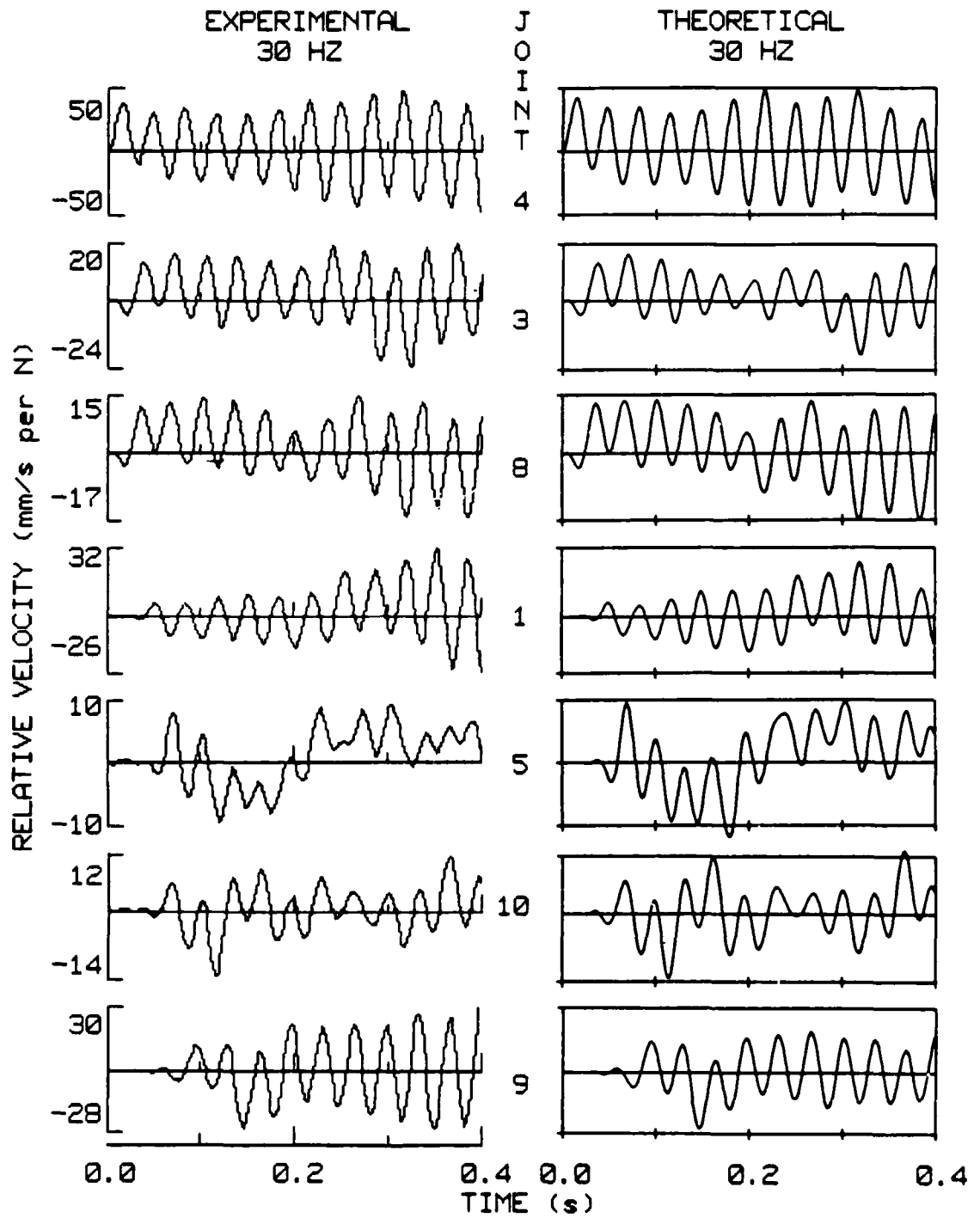


Fig. 4 Response to 30 Hz SAS force at joint 4 beginning at  $t = 0$  s. The nominal force amplitude was 0.337 N.

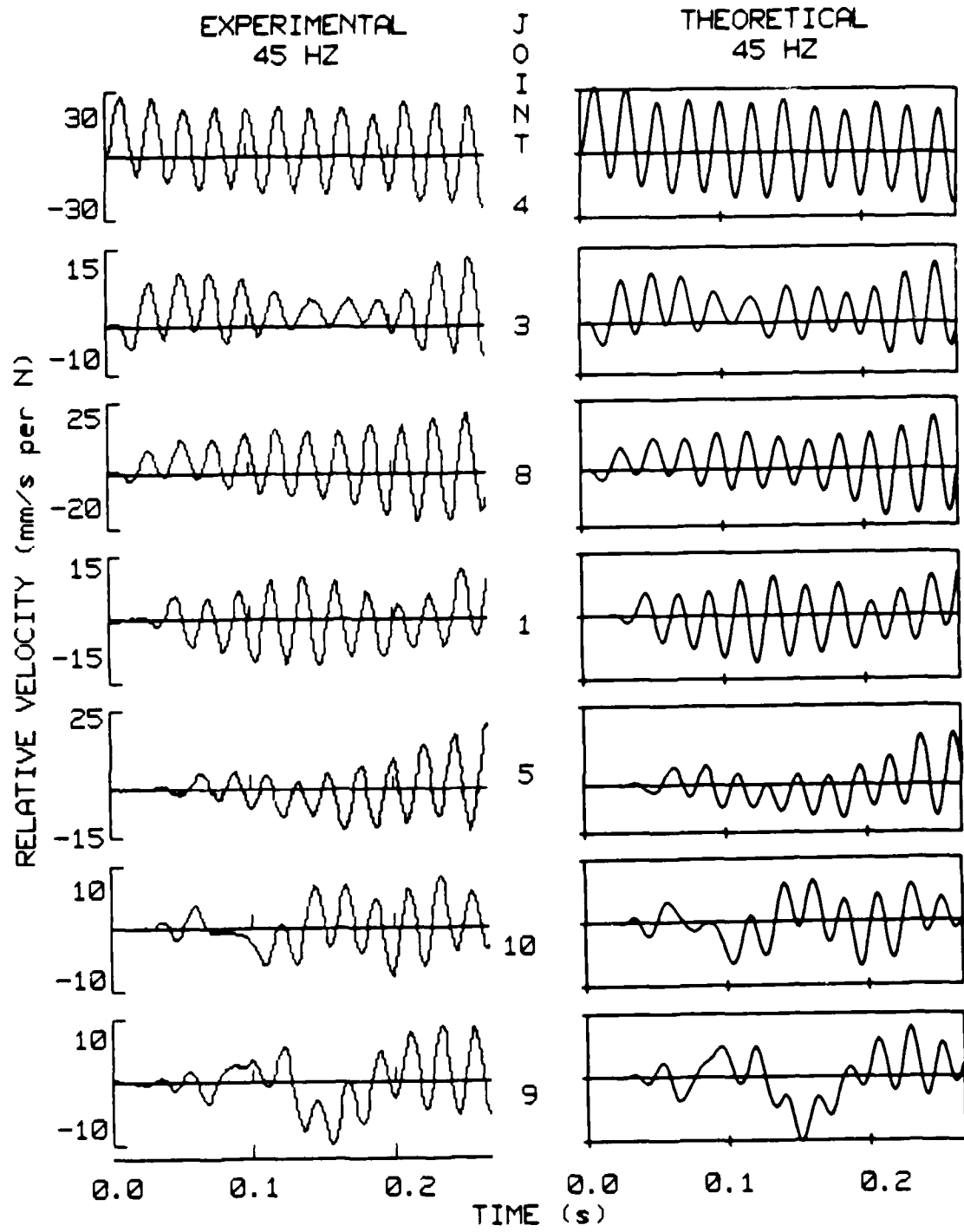


Fig. 5 Response to 45 Hz SAS force at joint 4 beginning at  $t = 0$  s. The nominal force amplitude was 0.338 N.

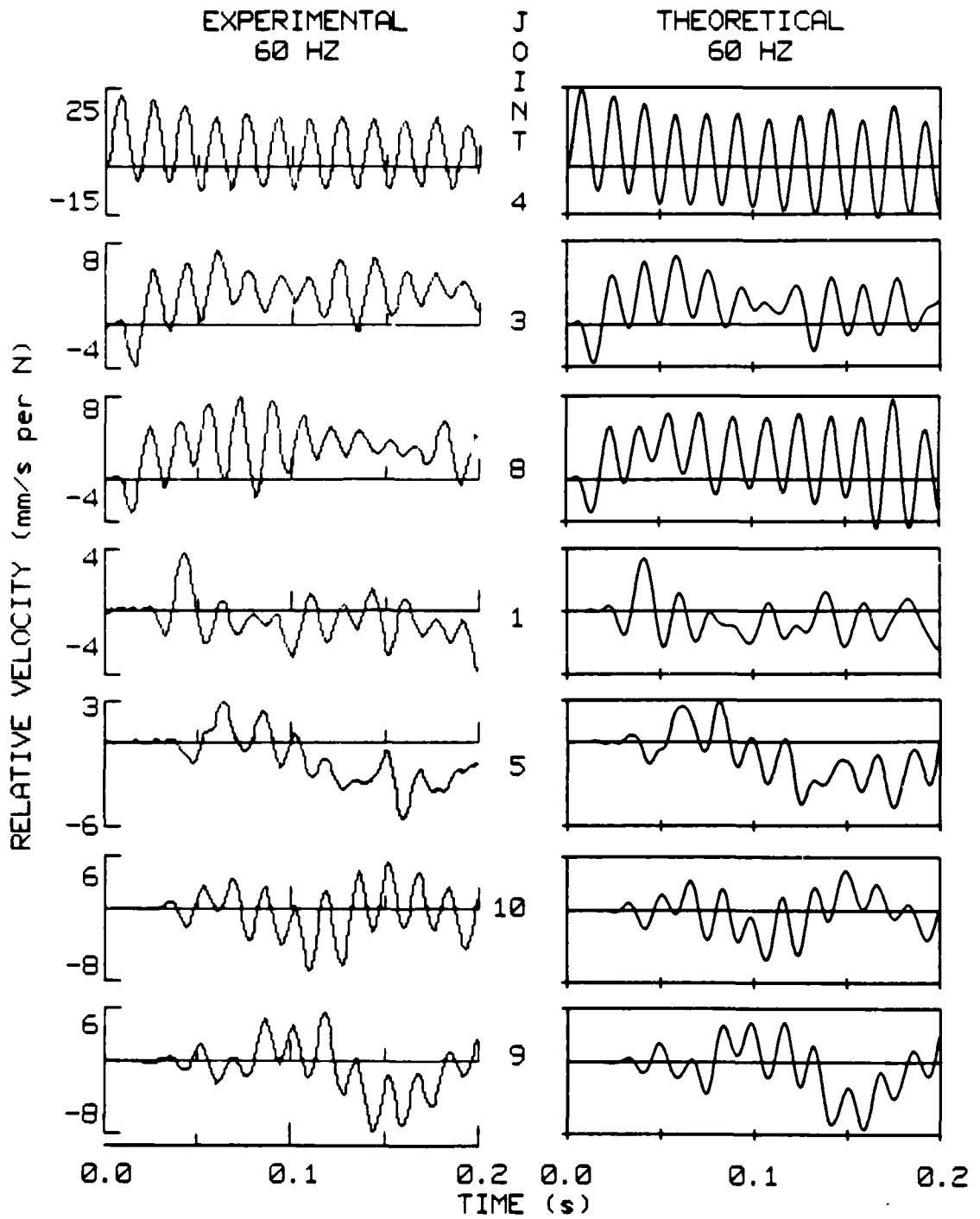


Fig. 6 Response to 60 Hz SAS force at joint 4 beginning at  $t = 0$  s. The nominal force amplitude was 0.671 N.

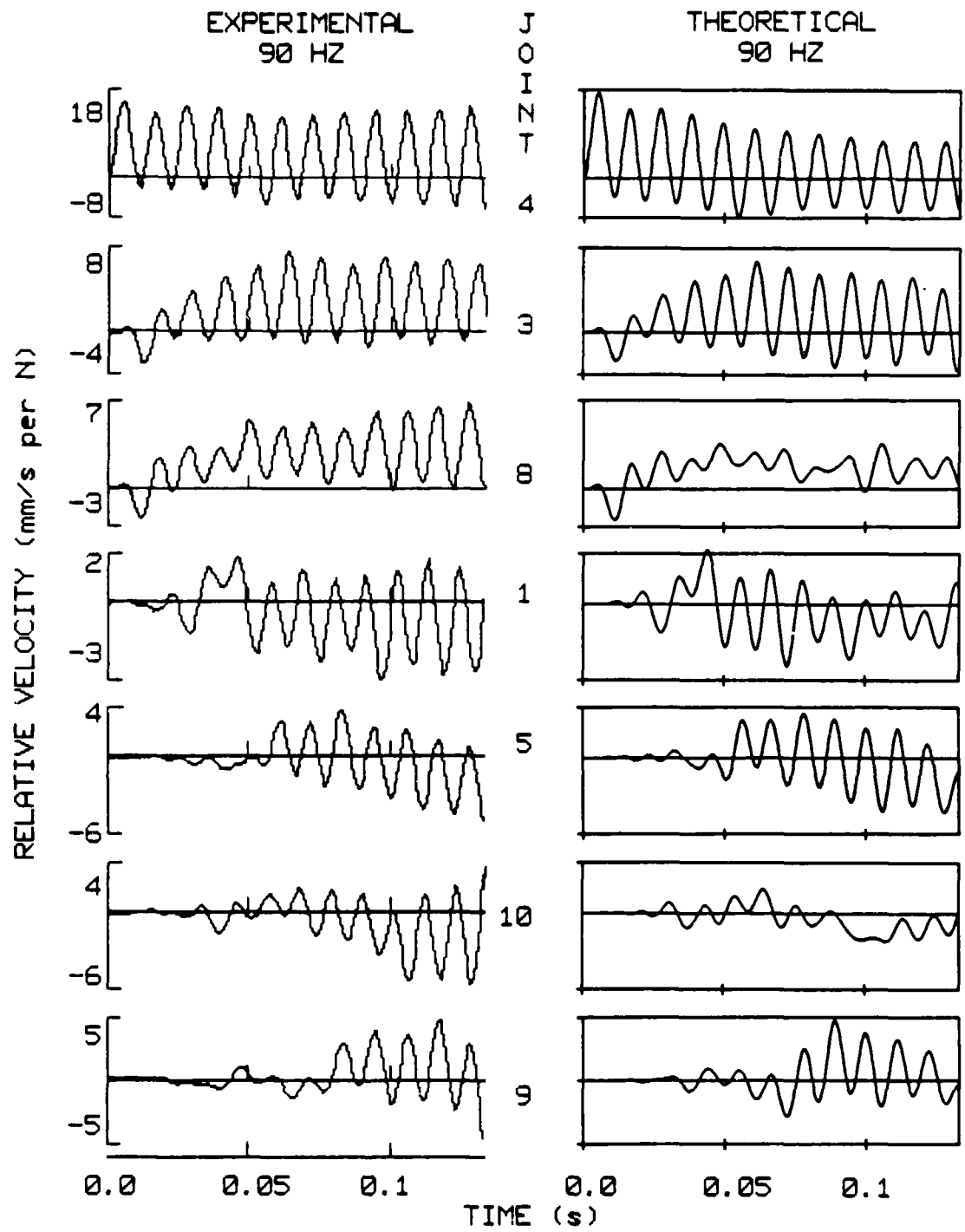


Fig. 7 Response to 90 Hz SAS force at joint 4 beginning at  $t = 0$  s. The nominal force amplitude was 0.840 N.

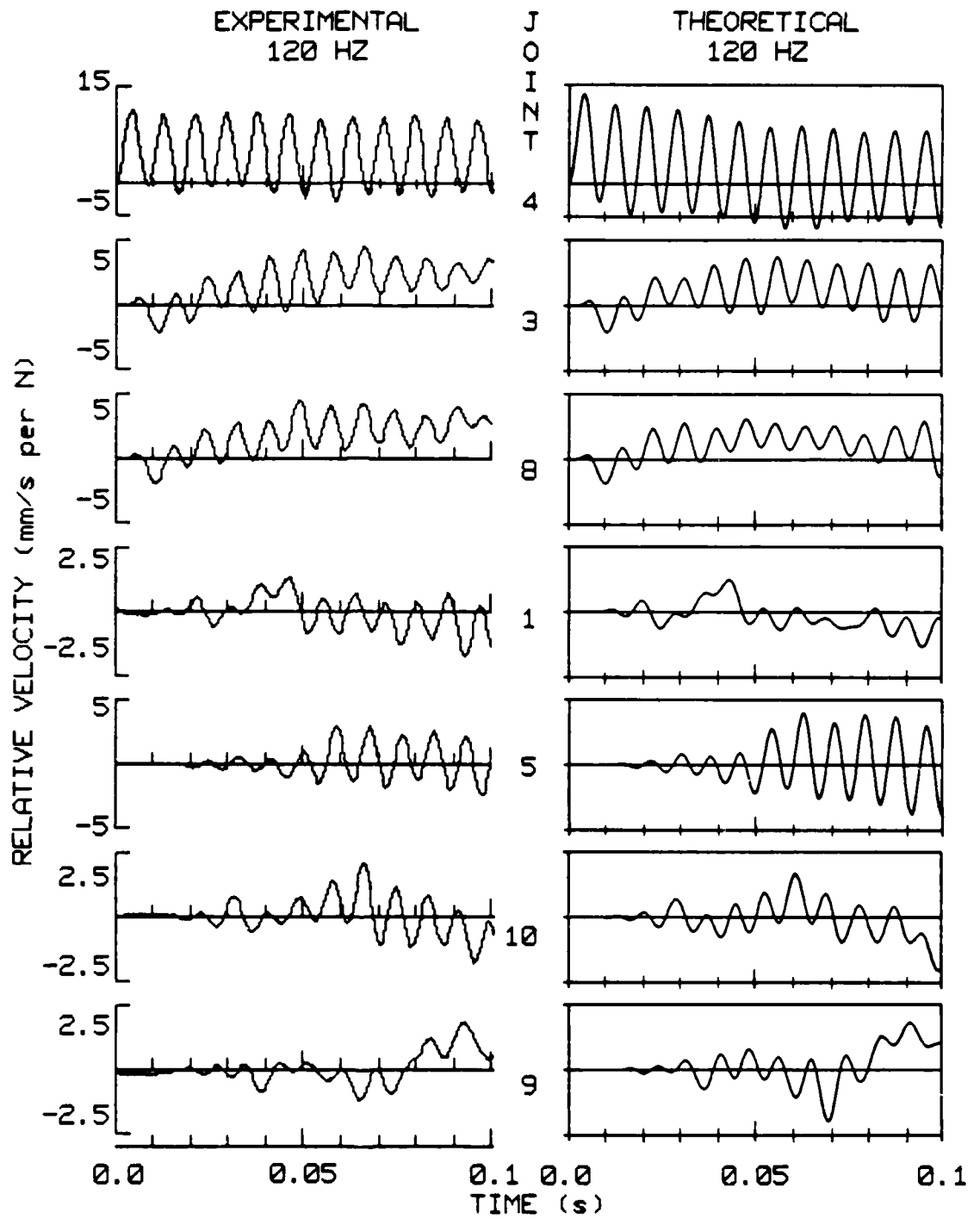


Fig. 8 Response to 120 Hz SAS force at joint 4 beginning at  $t = 0$  s. The nominal force amplitude was 1.008 N.

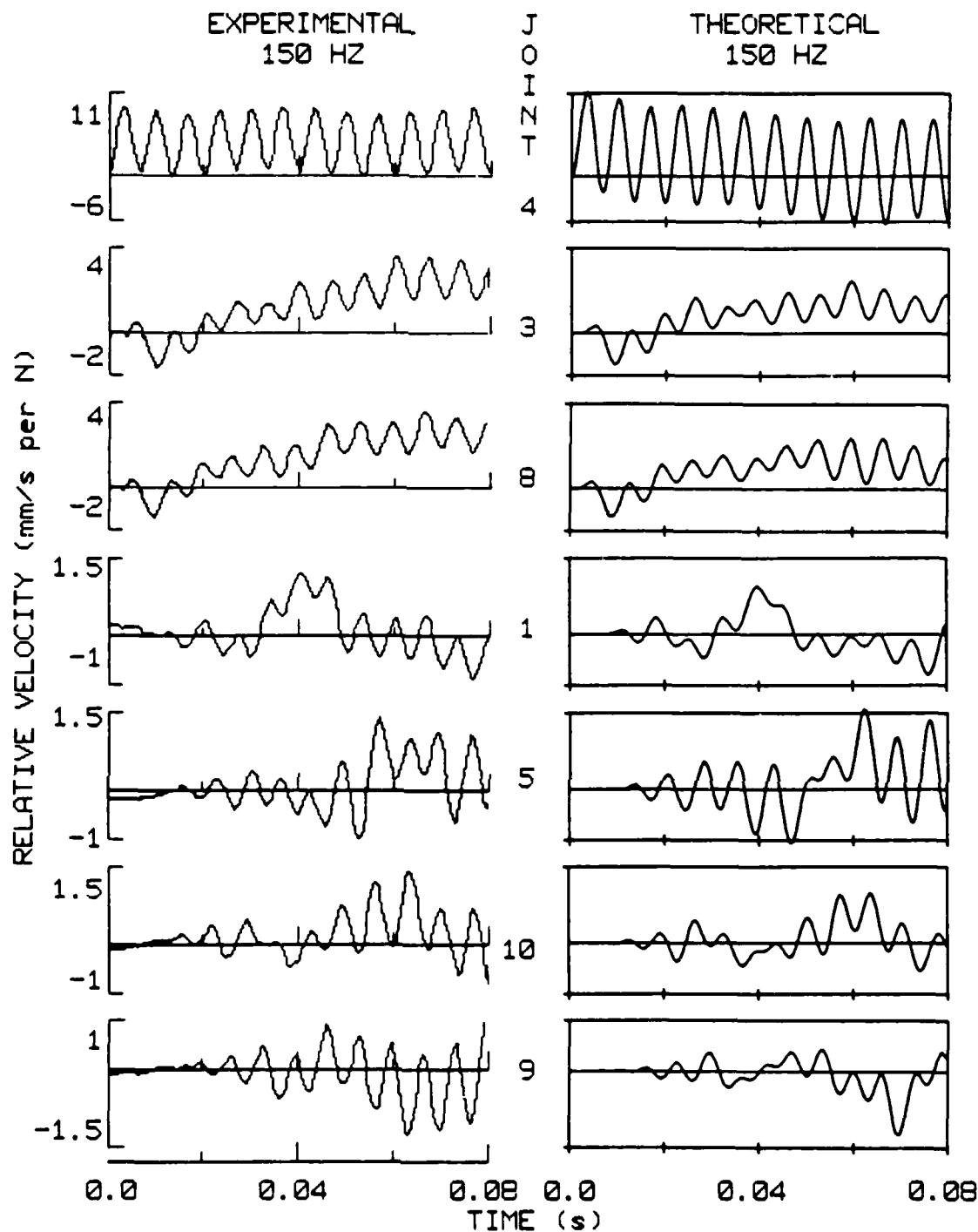


Fig. 9 Response to 150 Hz SAS force at joint 4 beginning at  $t = 0$  s. The nominal force amplitude was 1.174 N.

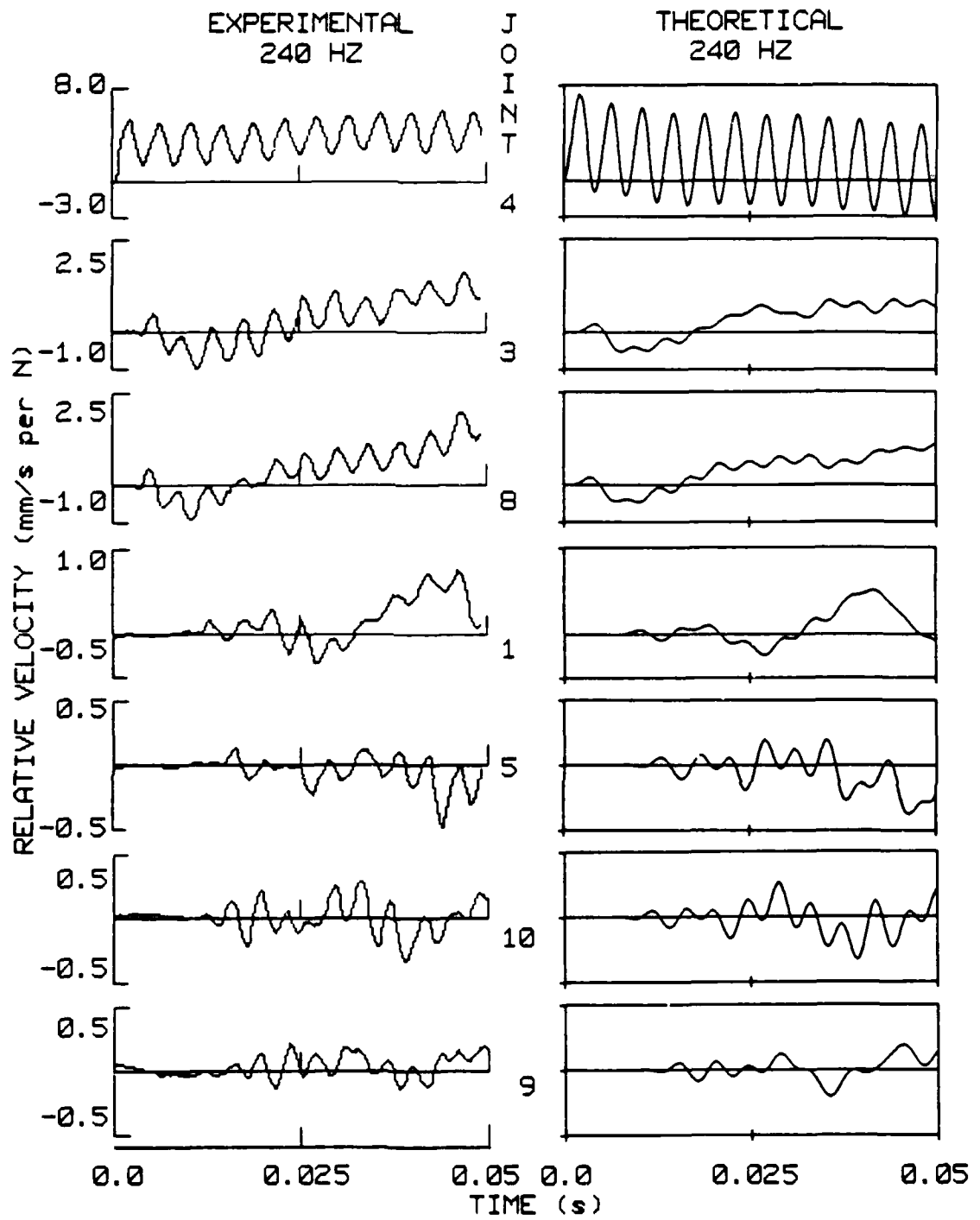


Fig. 10 Response to 240 Hz SAS force at joint 4 beginning at  $t = 0$  s. The nominal force amplitude was 1.346 N.

90 HZ SAS FORCE AT JOINT 4  
RELATIVE VELOCITY AT JOINT 1

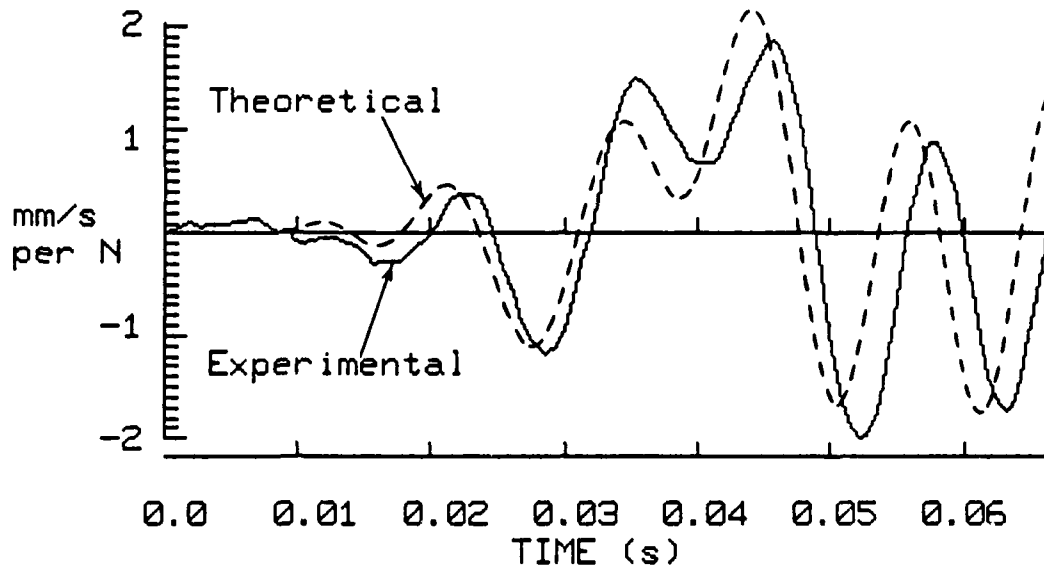


Fig. 11 Joint 1 response (expanded from Fig. 7) illustrating wave speed predicted by theory to be higher than measured.

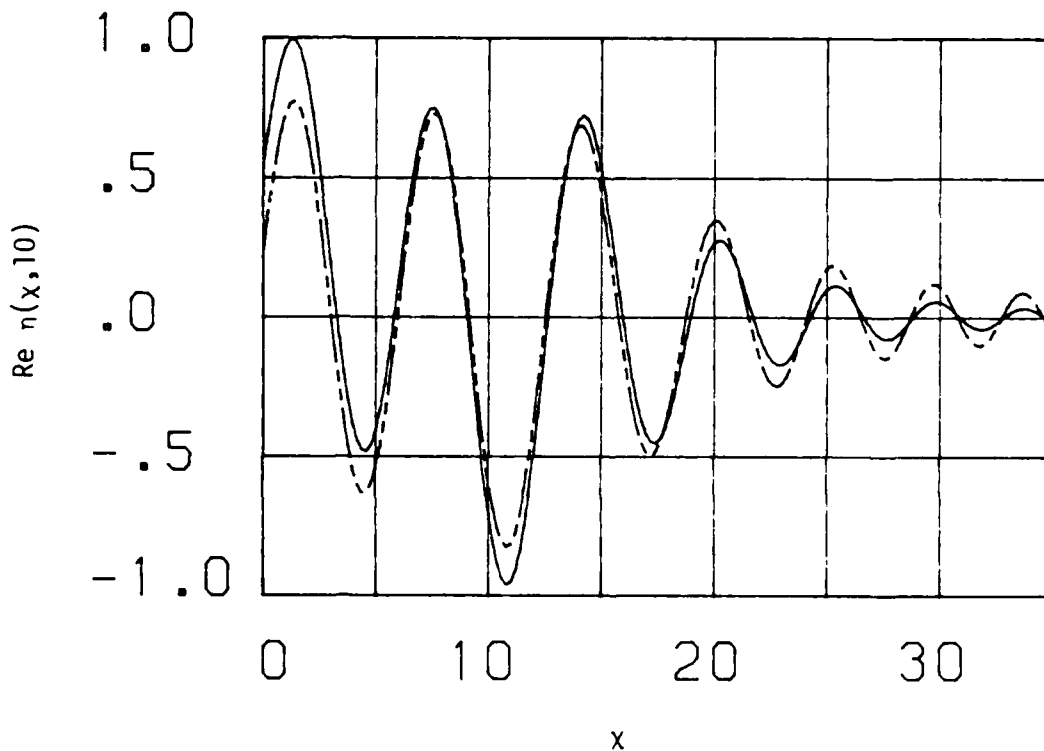


Fig. 12 Dimensionless displacement at  $\tau = 10$  (solid curve) and dominant third term of solution Eq. 2 (broken curve).

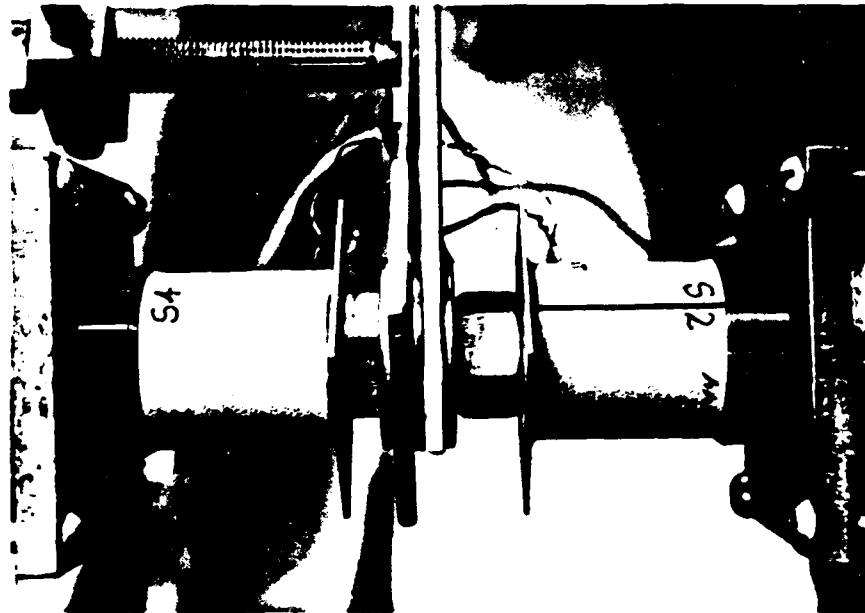


Fig. 13 Bolted joint 4, photographed from the right and above joint 4 in Fig. 1; displacement sensor (upper left), force actuator (lower left), and velocity sensor (right).

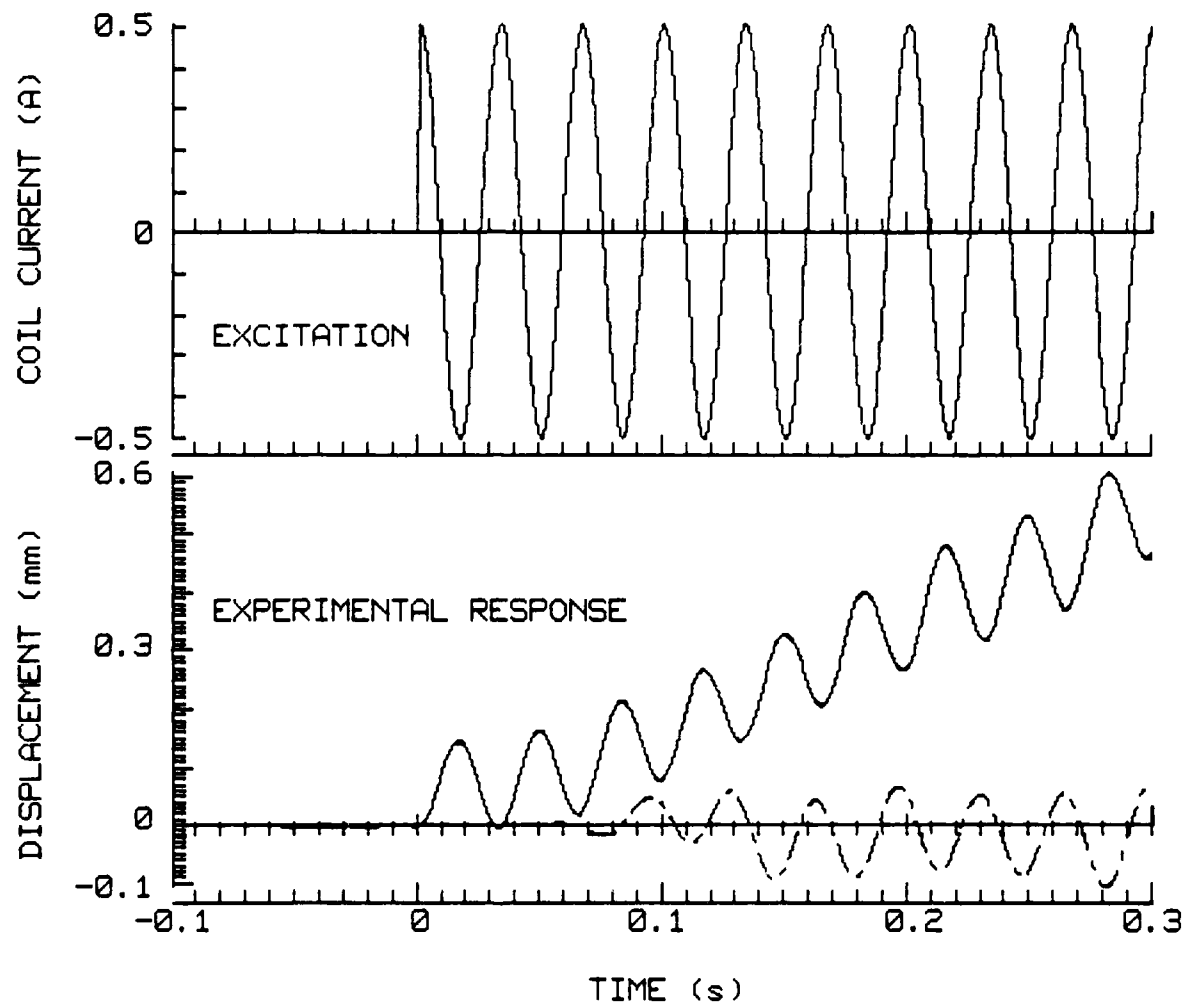


Fig. 14 Experimental excitation and response for a 30 Hz SAC current excitation at joint 4. The nominal excitation force amplitude was 0.672 N. The solid curve on the lower graph is joint 4 response, and the broken curve is joint 9 response.

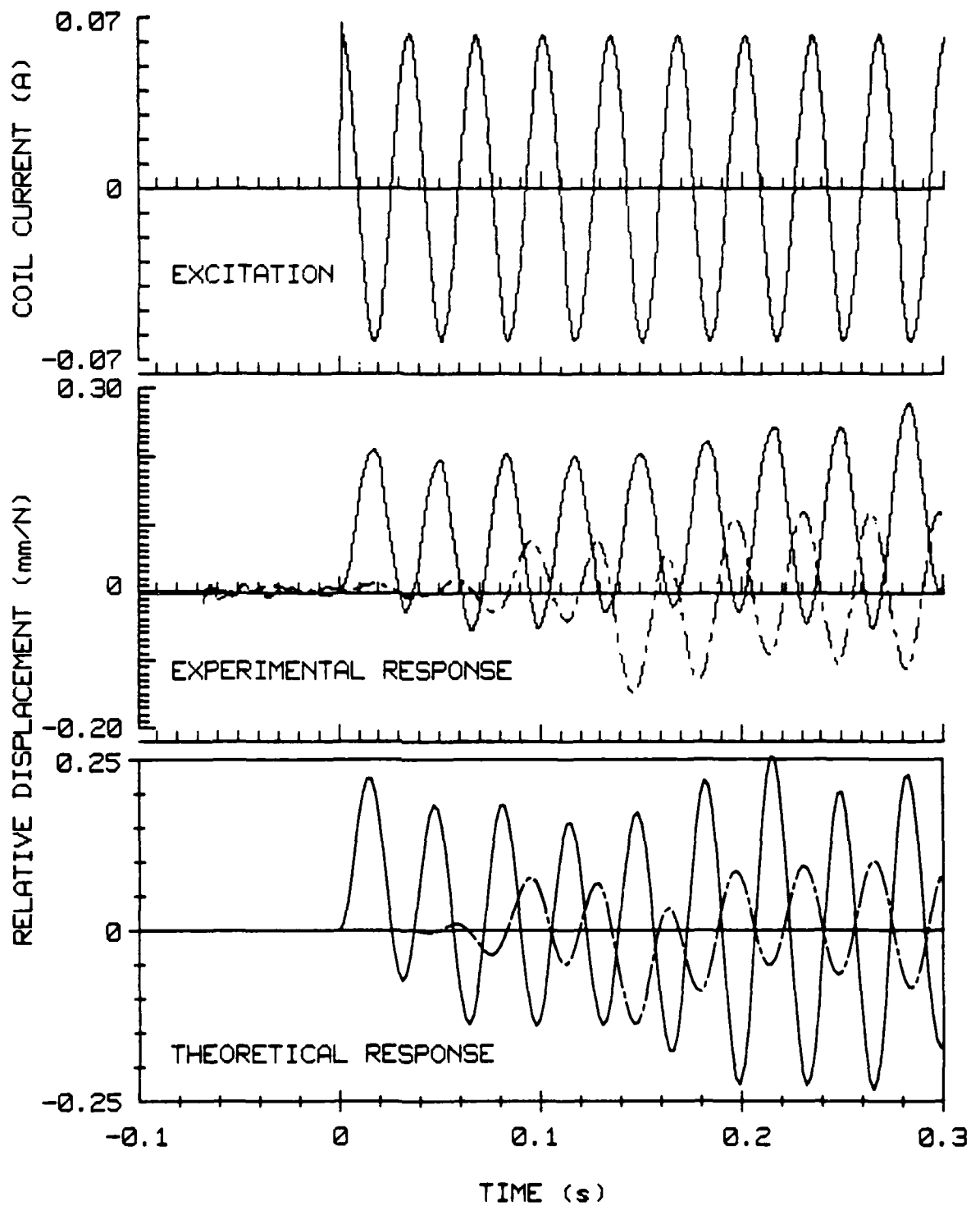


Fig. 15 Experimental excitation and both experimental and theoretical response for a 30 Hz SAC current excitation at joint 4. The nominal excitation force amplitude was 0.0839 N. The solid curves on the response graphs are joint 4 responses, and the broken curves are joint 9 responses.

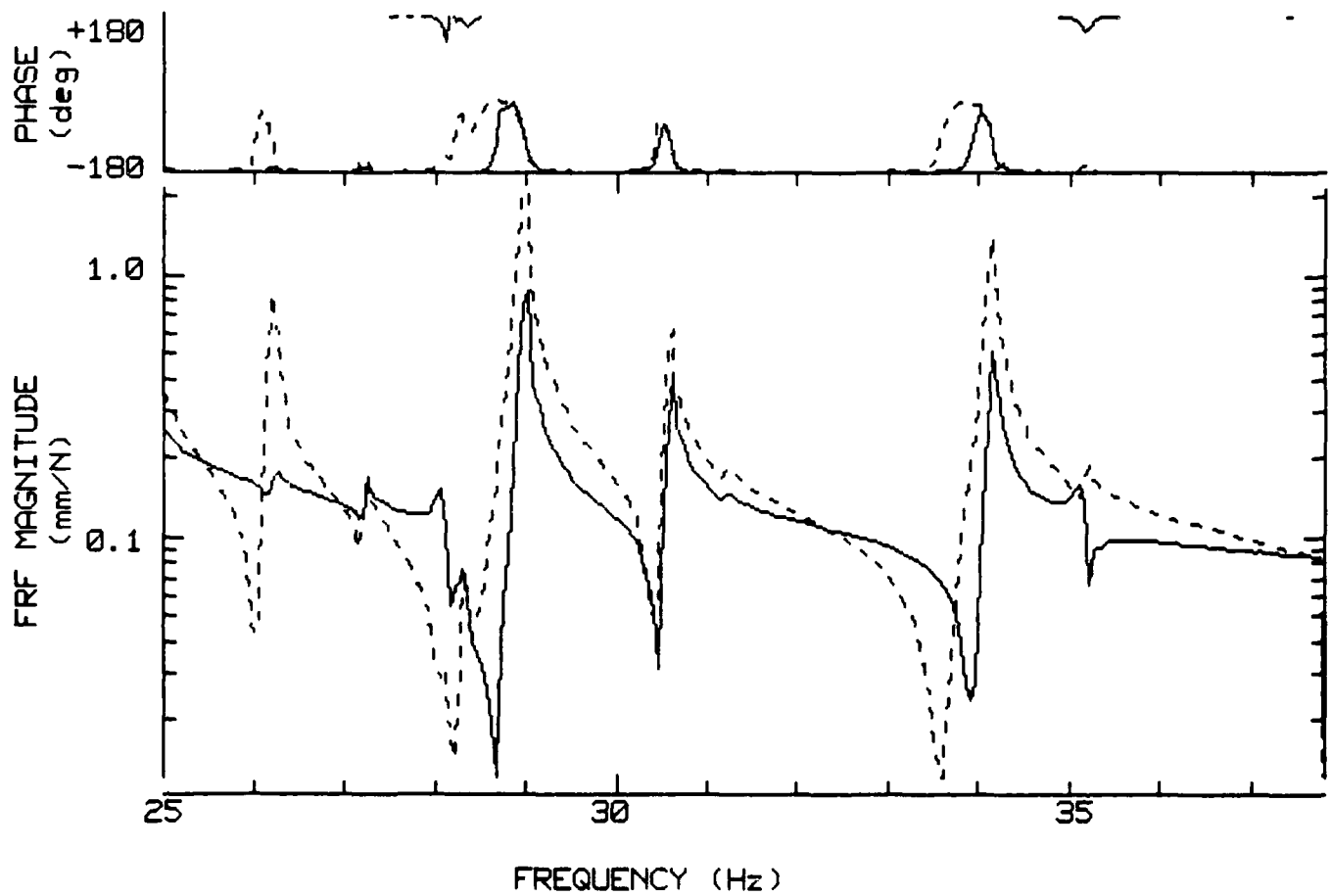


Fig. 16 Pendulous grid frequency response functions for force excitation at joint 4. The solid curves are for displacement measured directly by the proximity probe positioned 51 mm from joint 4. Velocity response at joint 4 was measured by the sensor shown on Fig. 13, and the velocity FRF was divided by  $i2\pi f$  to produce the joint 4 displacement FRF plotted as broken curves.

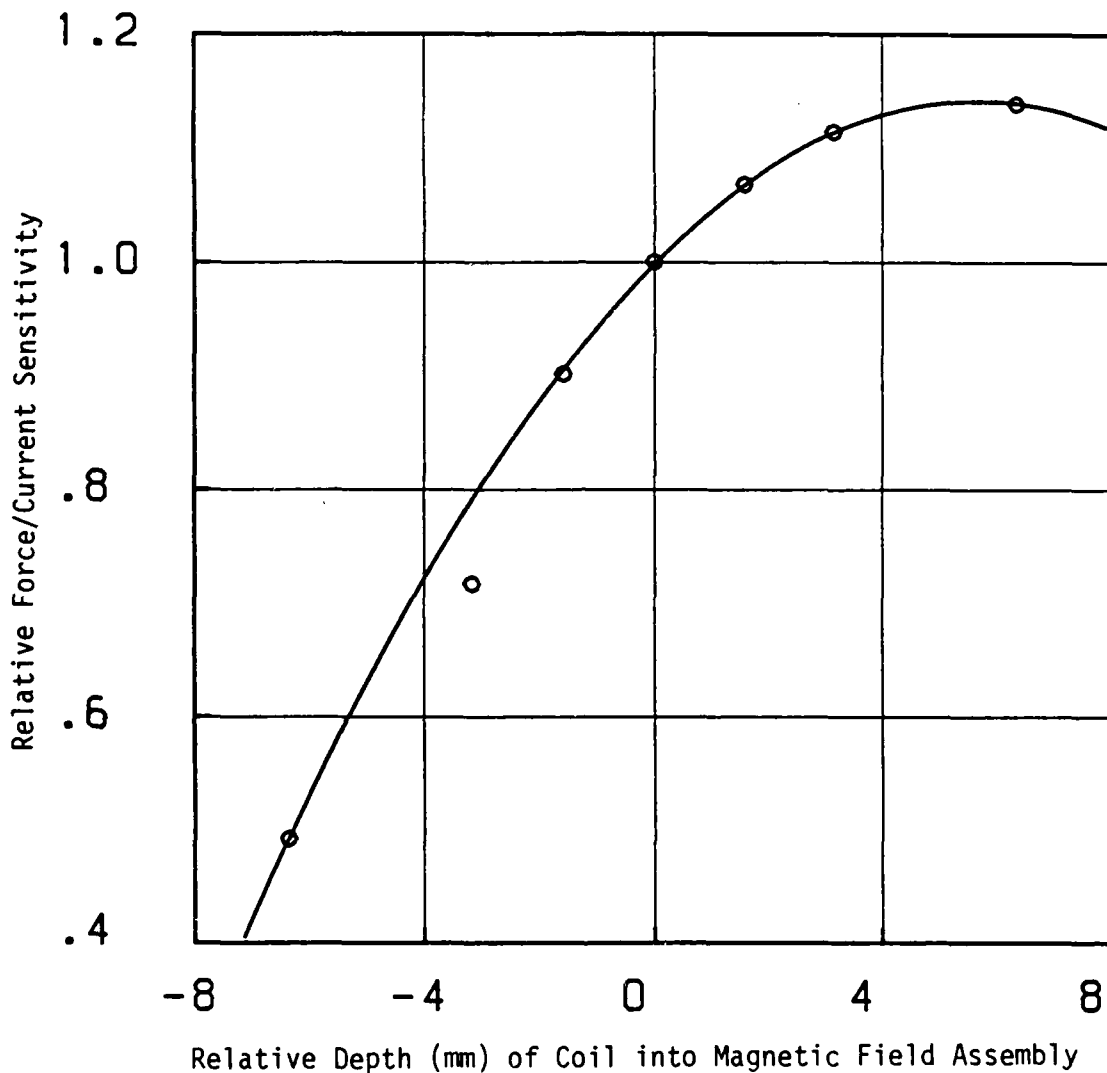


Fig. 17 Sensitivity of a magnet-coil force actuator nominally identical to the actuator used at joint 4. The sensitivity at 0 mm relative depth (the static position shown on Fig. 13) is 1.45 N/A. Measured data points are shown, and the curve is a least-squares parabola fit to six of the seven data points.

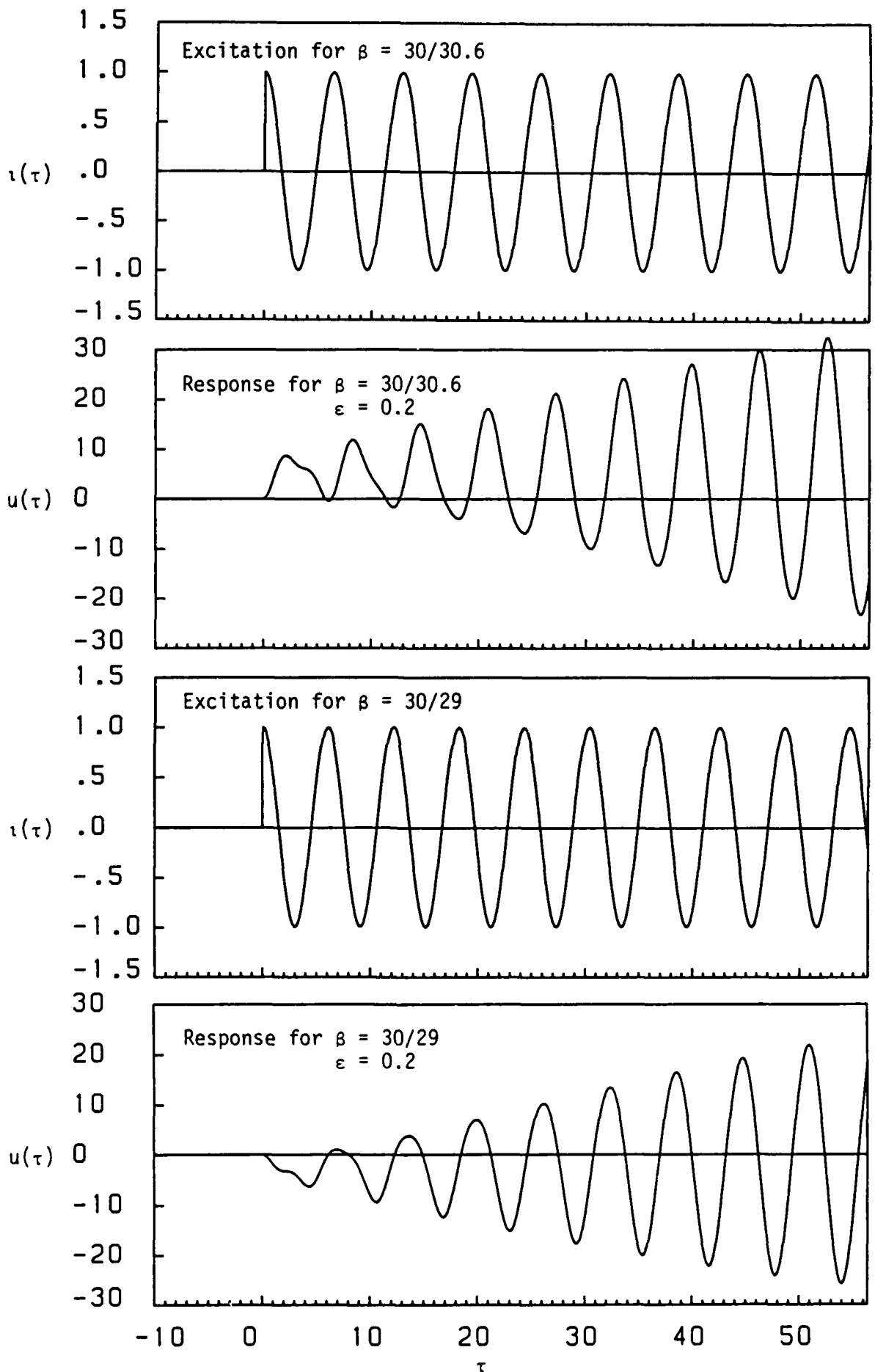
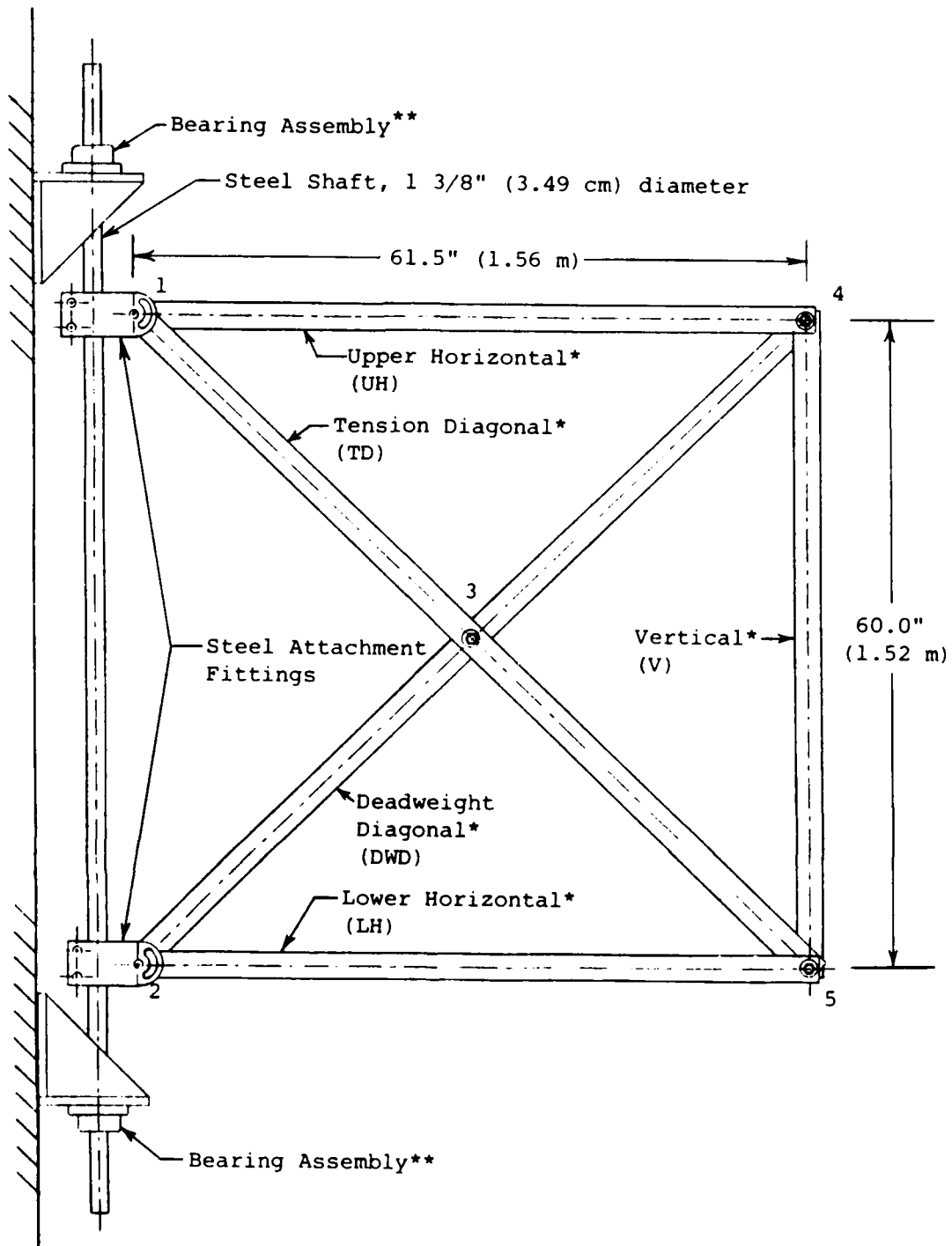


Fig. 18 Numerical evaluations of Eq. 8b for excitation current  $i(\tau)$  and Eqs. 9 for response displacement  $u(\tau)$ .



\*Aluminum Beam Members  
 Alloy 6061-T6  
 Nominal cross-section:  
 2" x 1/8"  
 (5.08 cm x 0.32 cm)

\*\*Ball Bearings  
 Make: SKF  
 Bearing No. 478207-106  
 Pillow Block Flange Unit  
 No. FYP-106  
 (Bearing seals and all  
 grease were removed to  
 reduce friction.)

Fig. 19 Line drawing of the slewing grid without any structure-borne sensors or actuators.



Fig. 20 Photograph of the slewing grid with all control hardware and excitation hardware attached. Single accelerometers are mounted at joints 2, 3 and 4. Two accelerometers attached to a horizontal bar are mounted at joint 5. Reaction wheels with flywheel axes oriented vertically are mounted at joints 1, 2, 3 and 5. A reaction wheel with flywheel axis oriented horizontally is mounted at joint 4. A noncontacting force excitation actuator identical to that of Fig. 13 is located on the DWD member midway between joints 3 and 4, and another is located on the LH member at the  $3/4$ -length point outboard from joint 2 toward joint 5.

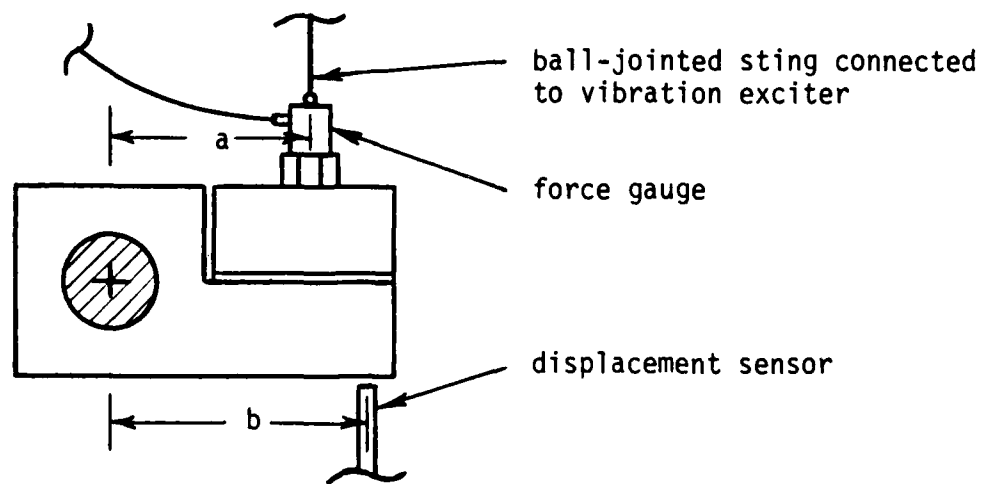


Fig. 21 Sketch from above of lower attachment fitting showing experimental setup for attempted measurement of the rotation fixture's moment of inertia.

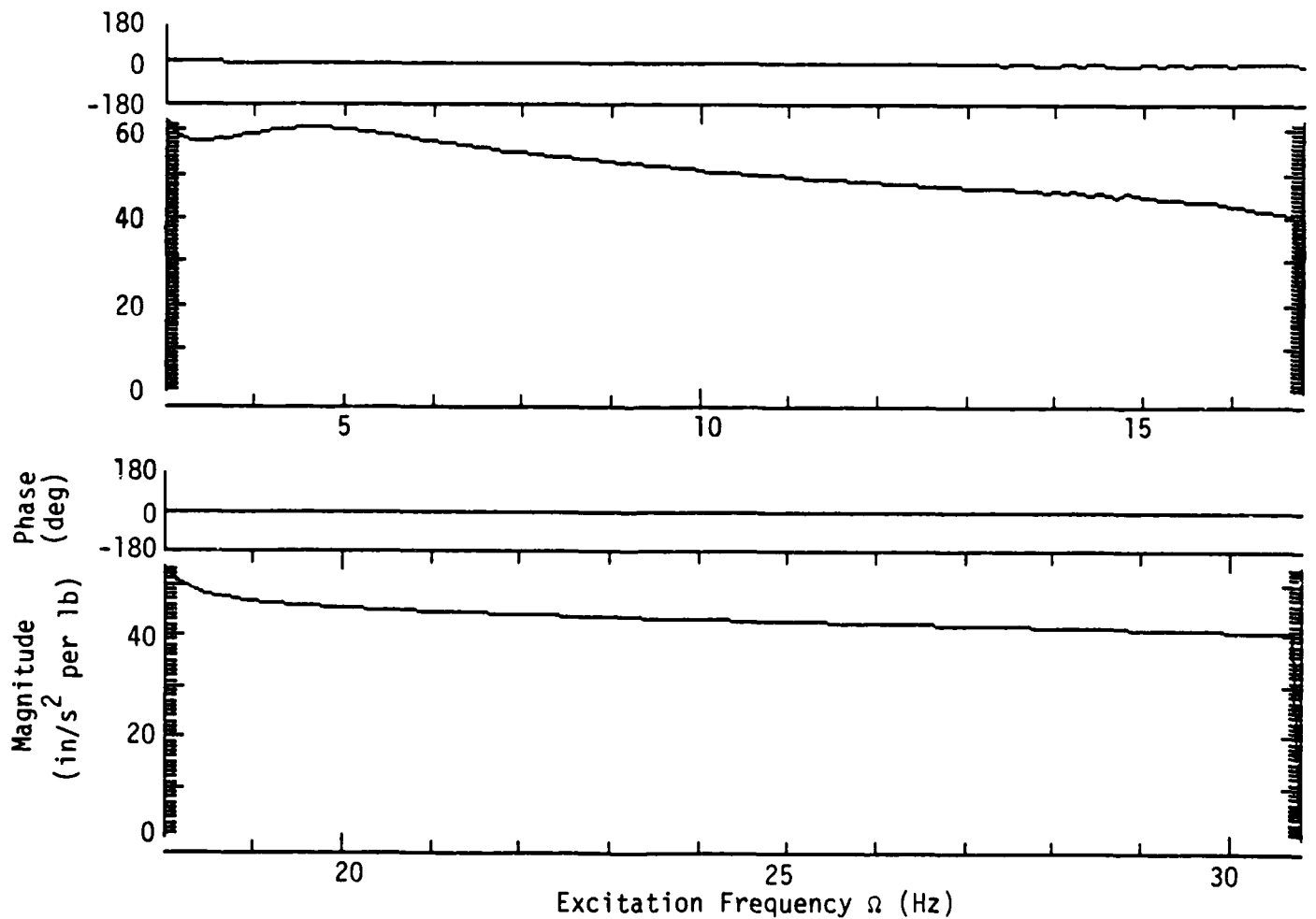


Fig. 22 Measured frequency response functions  $-\Omega^2 X/F$  for the rotation fixture with the experimental setup of Fig. 21.

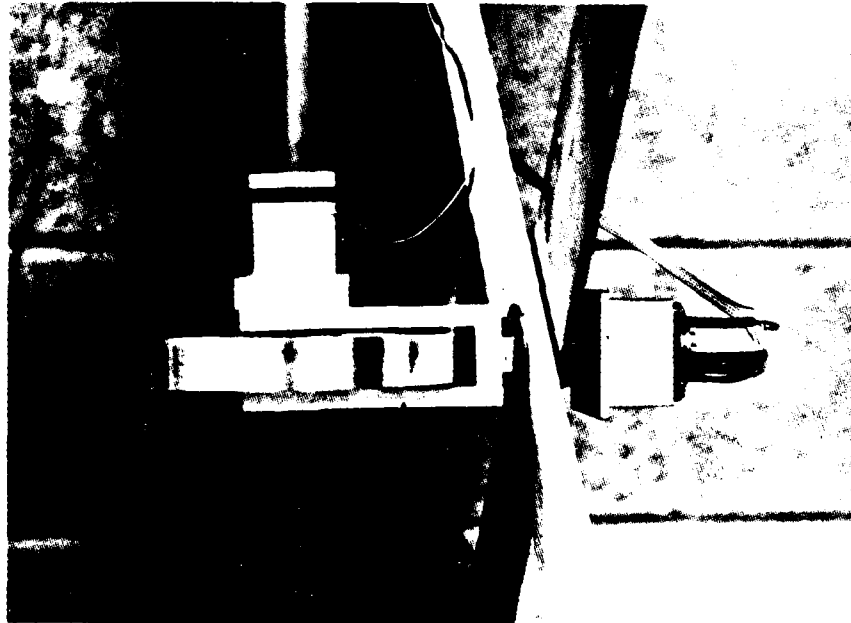


Fig. 23 Control hardware mounted at joint 3: reaction wheel at left, and servo accelerometer in mounting adapter at right.

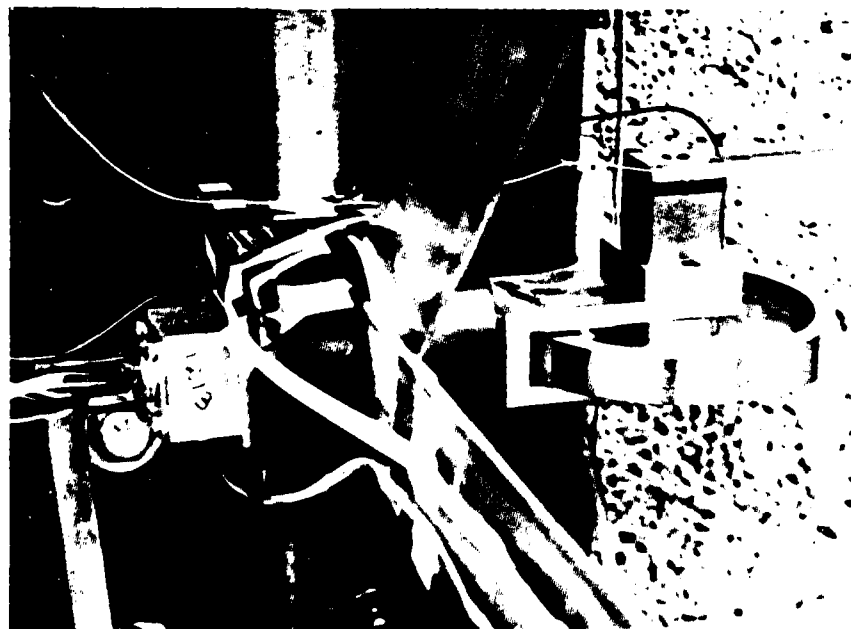


Fig. 24 Control hardware mounted at joint 2: servo accelerometer in mounting adapter at left, and reaction wheel at right.

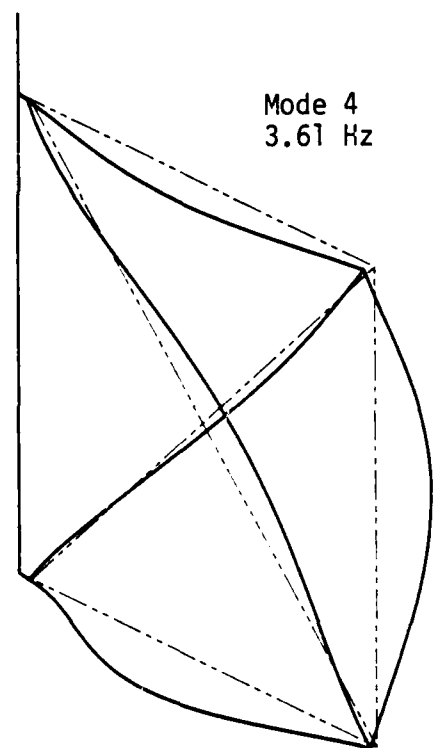
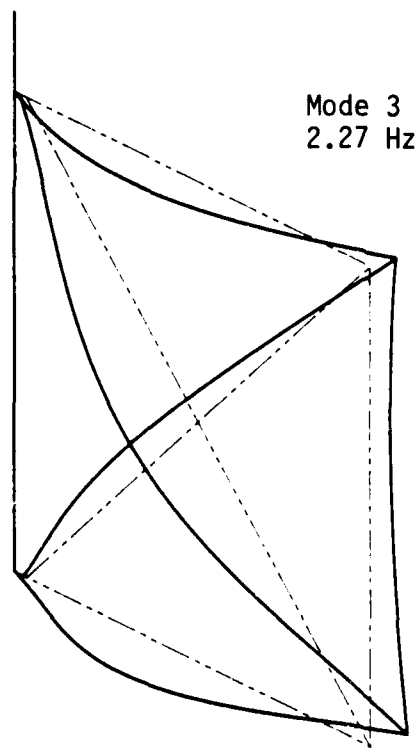
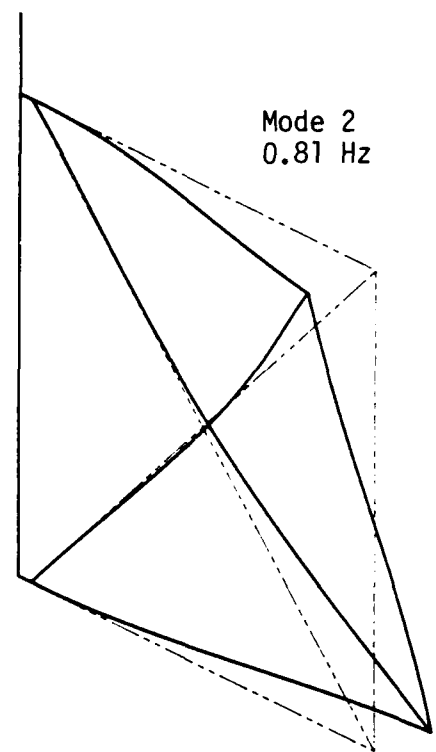
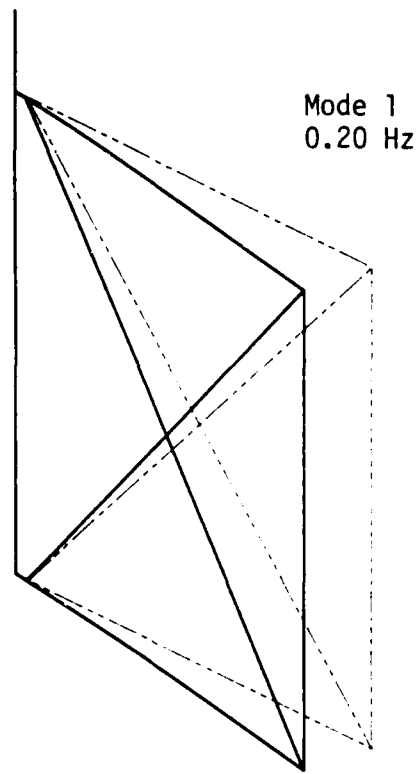


Fig. 25a First four theoretical vibration modes of the slewing grid.

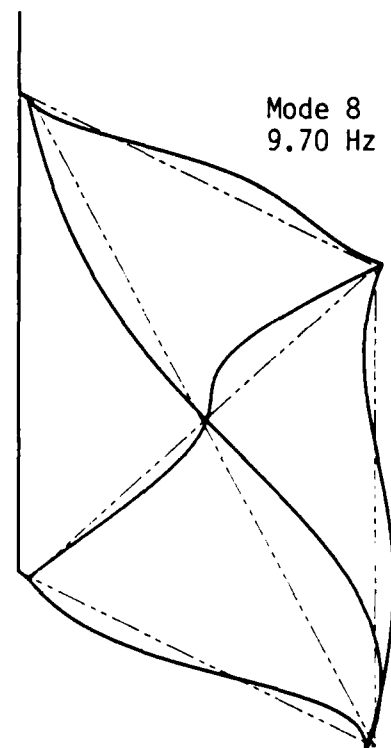
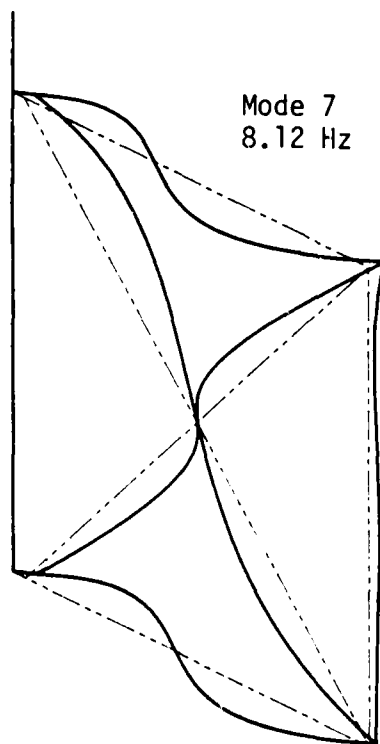
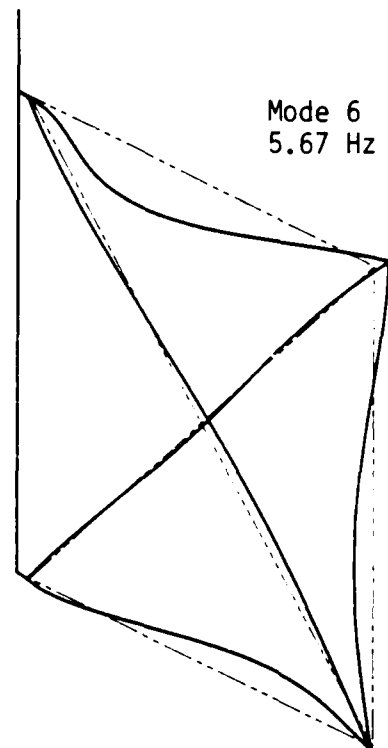
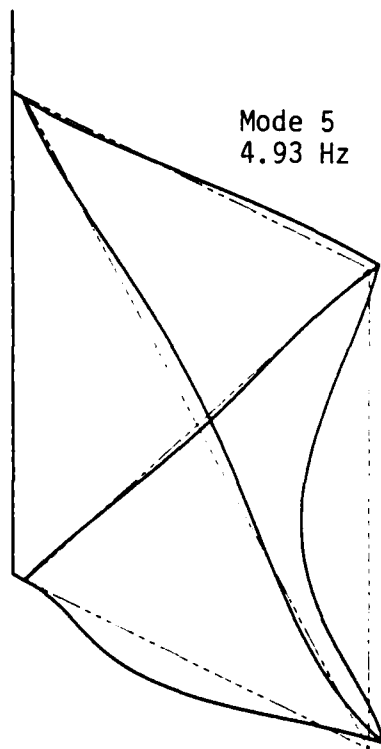


Fig. 25b Second four theoretical vibration modes of the slewing grid.

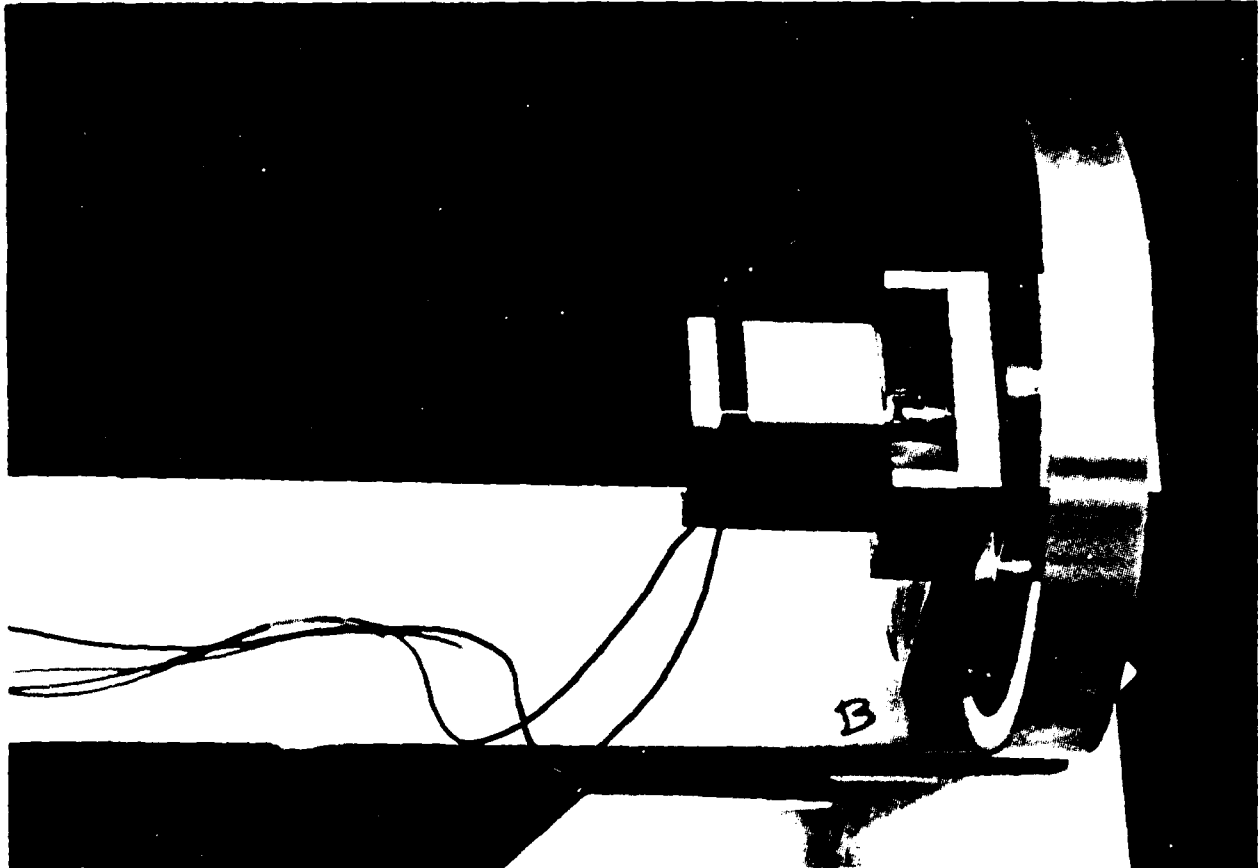


Fig. 26 Reaction wheel actuator mounted at joint 4 with flywheel axis oriented horizontally. The torque motor is at left and the flywheel is at right. Both are attached to a frame which, in turn, is attached to joint 4 by a 10-32 screw through an axial hole drilled in the joint bolt.

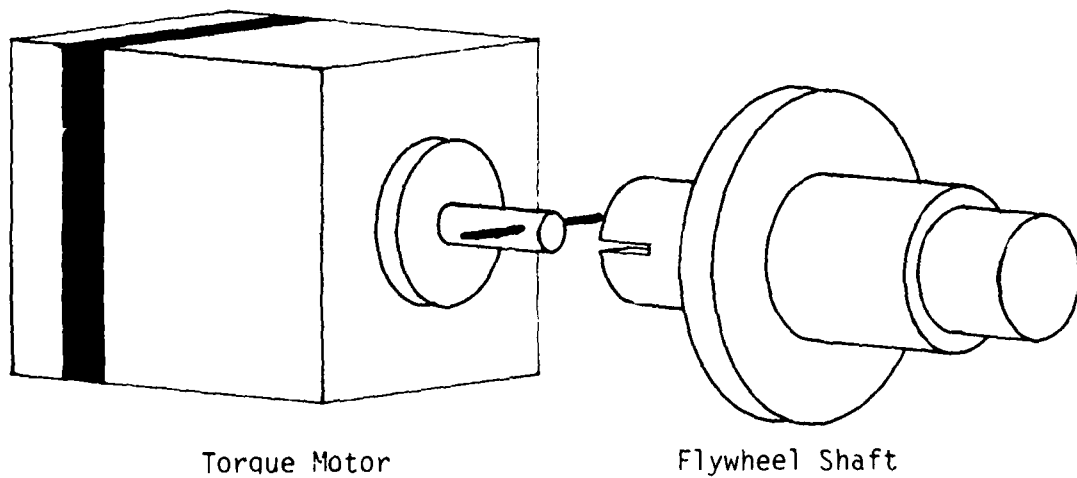


Fig. 27 Sketch of mechanical coupling between torque motor and flywheel shaft.

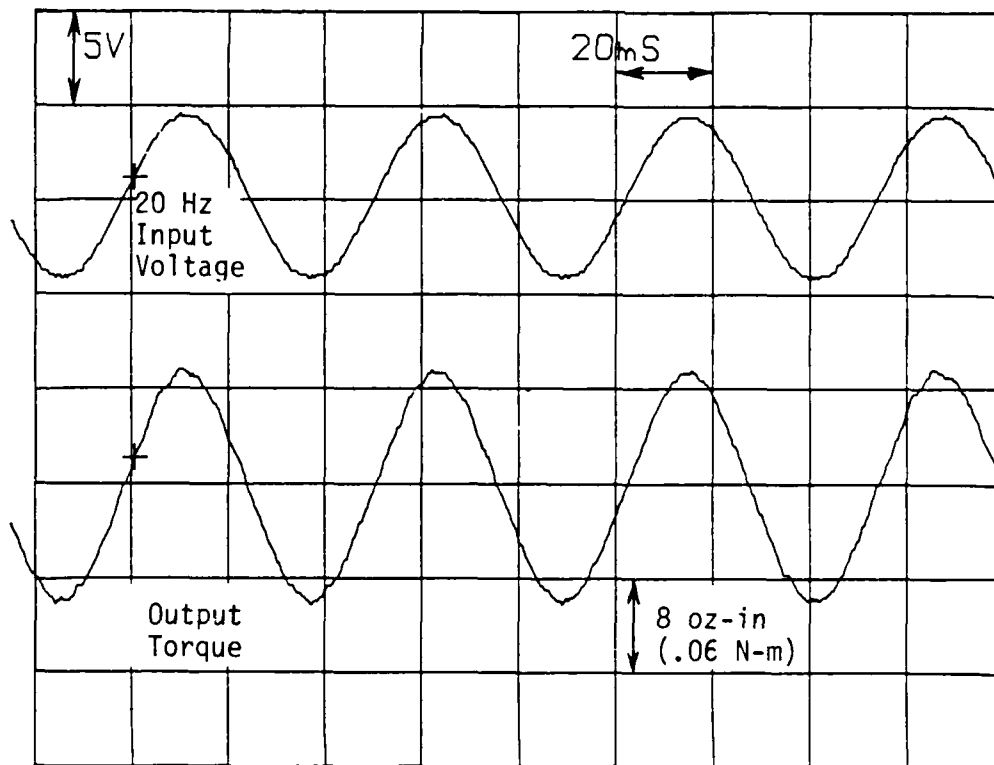


Fig. 28 Oscilloscope record of nearly ideal torque generated by actuator #5.

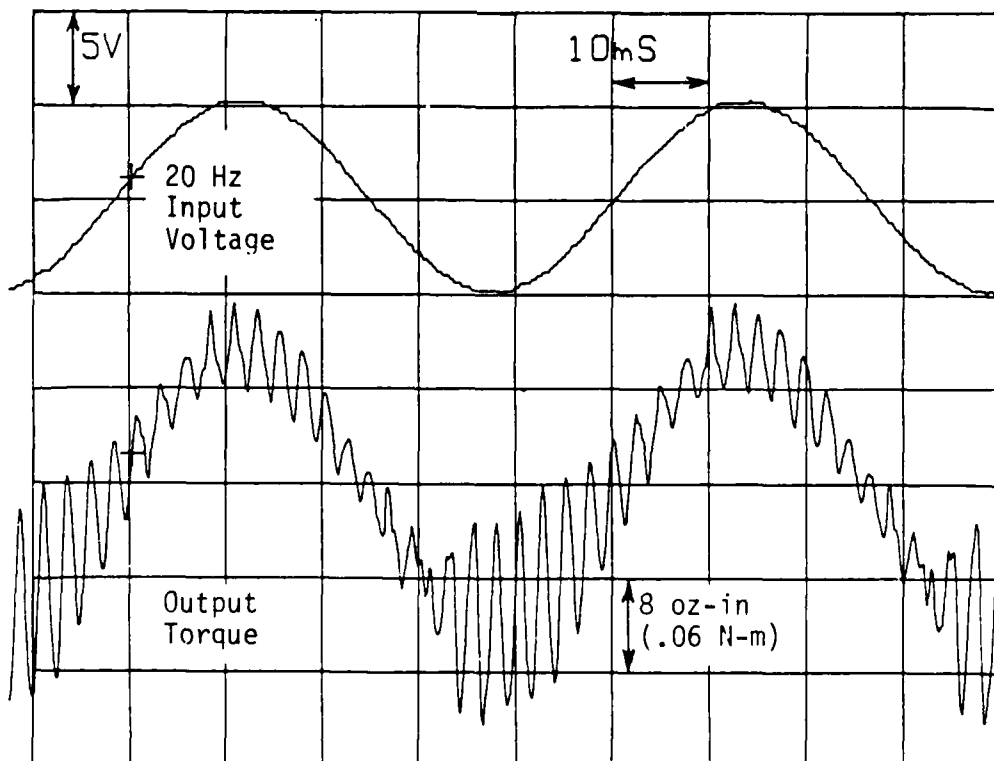


Fig. 29 Oscilloscope record of torque generated by actuator #5 with the mean flywheel position rotated  $90^\circ$  relative to the position for Fig. 28.

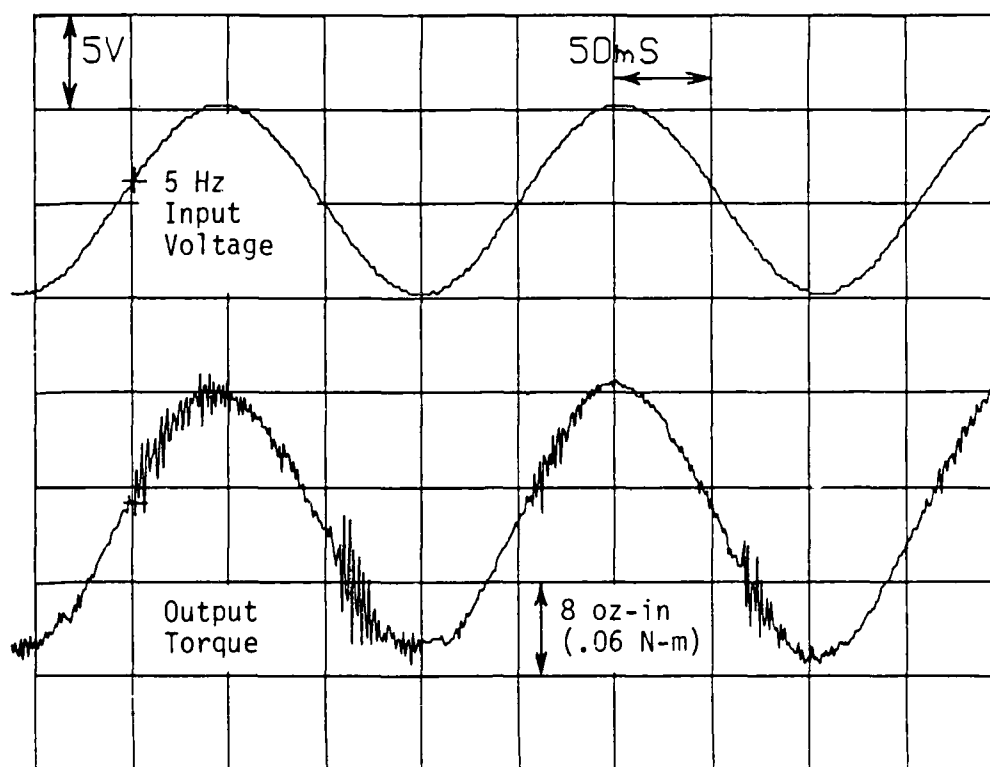


Fig. 30 Oscilloscope record of torque generated by actuator #5 with the mean flywheel position identical to that for Fig. 29, but with a lower driving frequency.

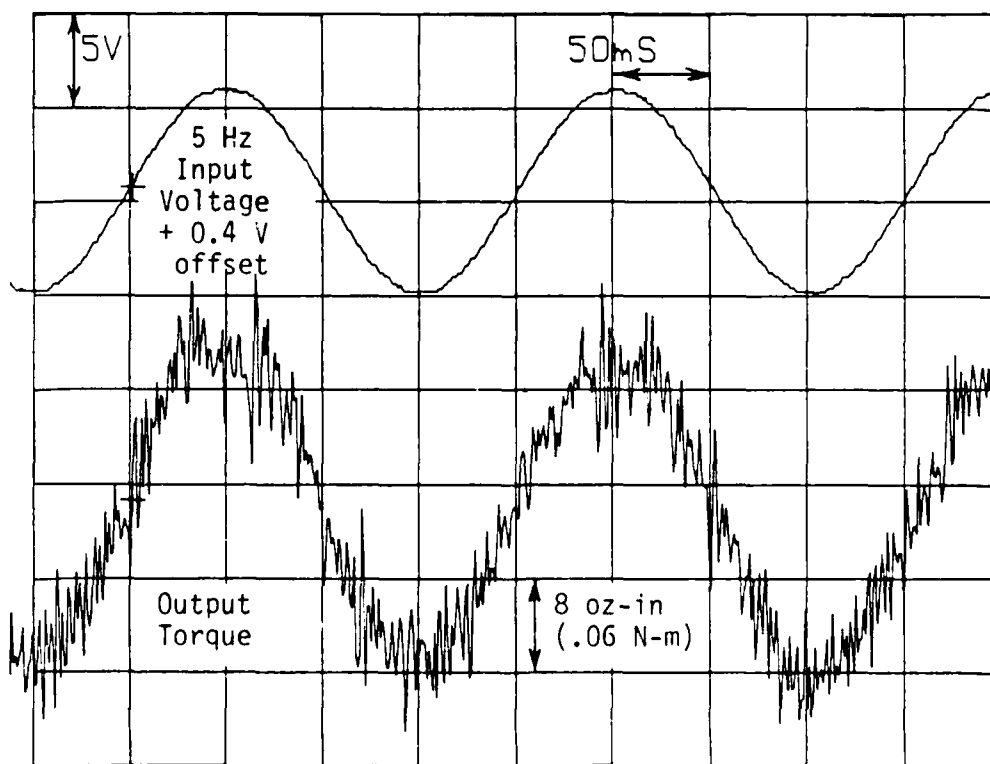


Fig. 31 Oscilloscope record of torque generated by actuator #4 operating with an angular velocity bias.

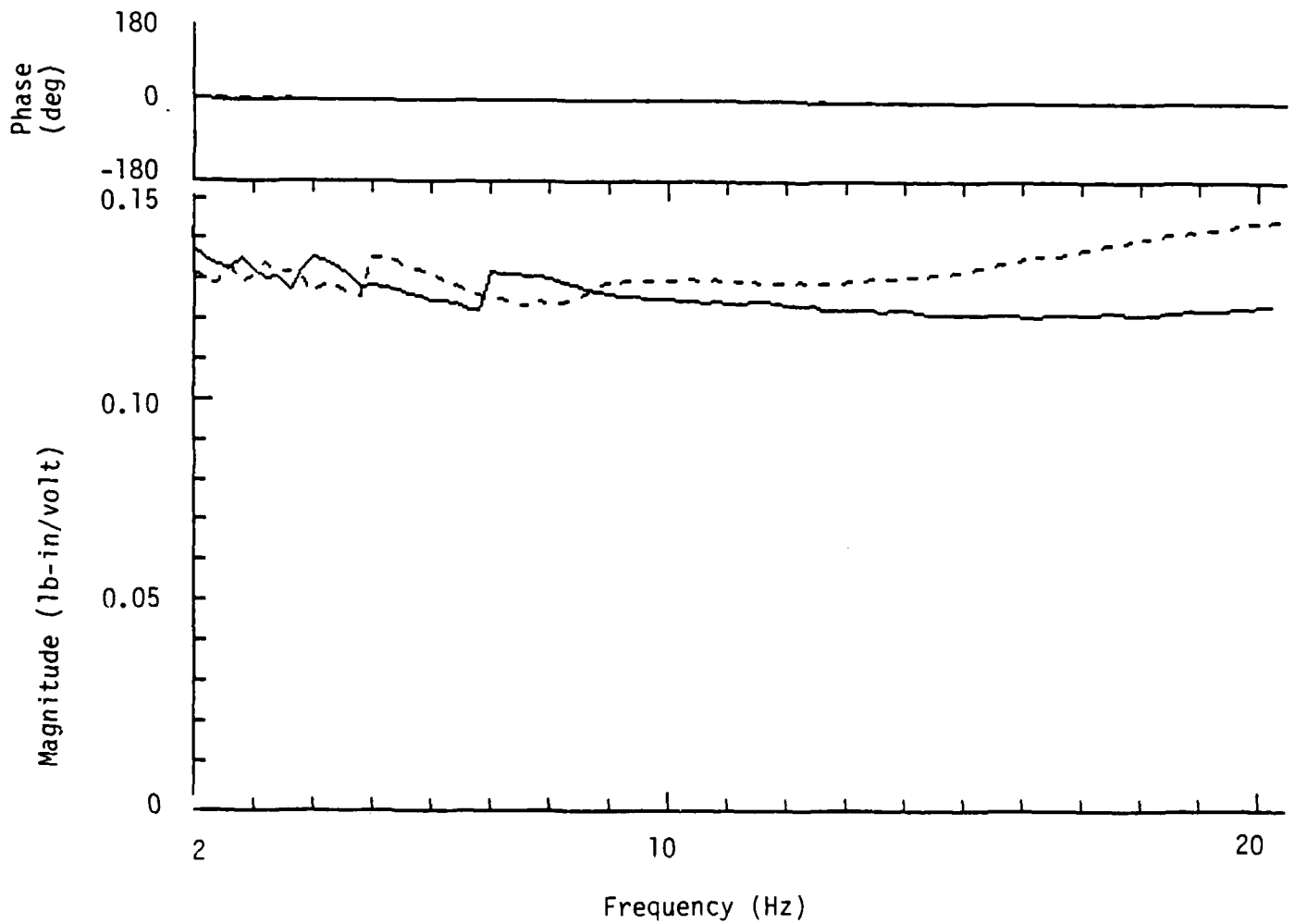


Fig. 32 Example calibration frequency response functions measured on actuator #5. The solid curves are for an incremental sine sweep in which the input level was 3 volts peak. The level of torque backlash observed on an oscilloscope during this sweep was low. The broken curves are for a sweep in which the input level was 2 volts peak. The level of torque backlash during this sweep was much higher.

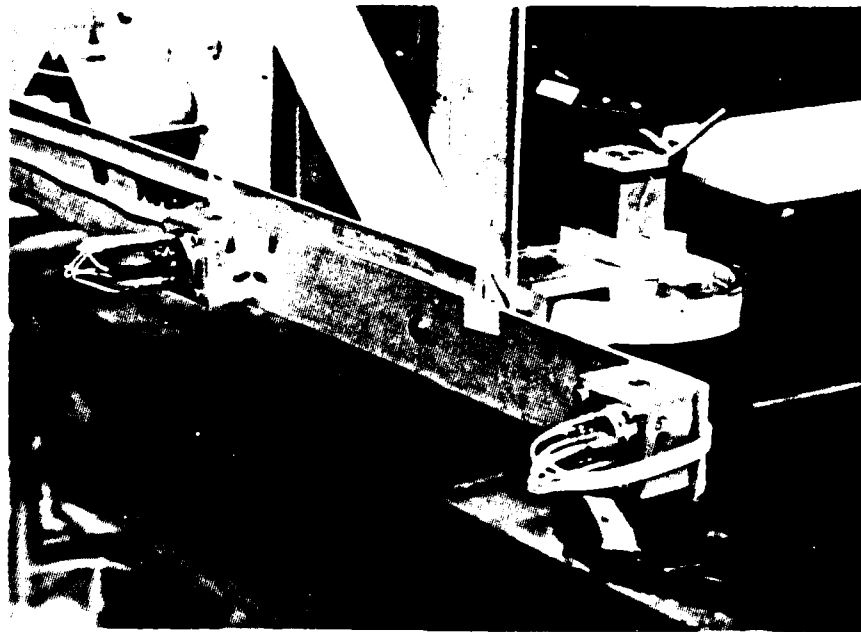


Fig. 33 Foreground: dual linear accelerometer arrangement at joint 5 to sense angular acceleration. Background left: excitation actuator at  $3/4$ -length point of LH member, consisting of magnetic field assembly and structure-borne coil (cf. Fig. 13). Background right: reaction wheel actuator at joint 5, with flywheel axis oriented vertically.

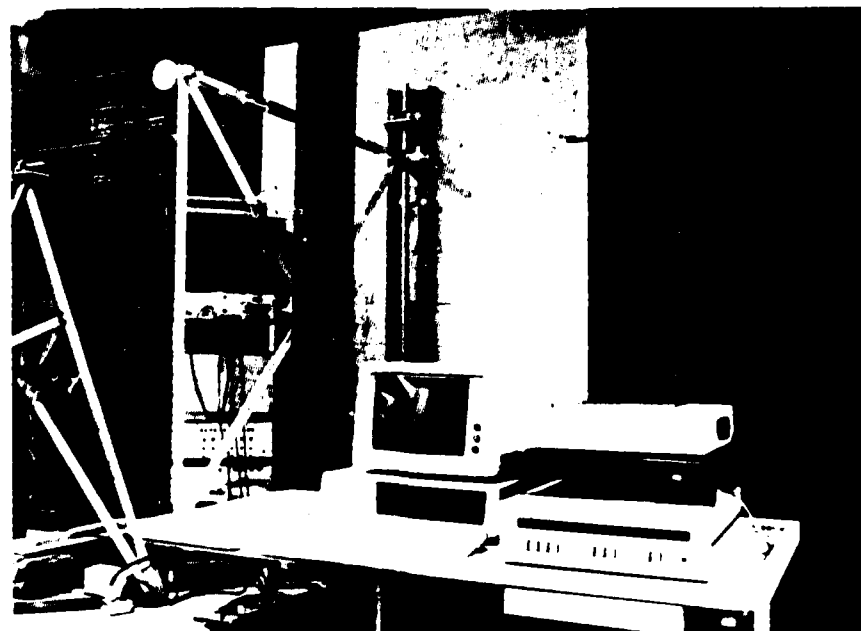


Fig. 34 Laboratory arrangement for the active damping experiment. The mobile rack holding the power amplifiers of the reaction wheel actuators is behind the slewing grid at left. The PC-1000 digital controller is shown on a mobile workstation in the foreground, along with its host IBM-PC computer and a printer. The STI-11/23 data acquisition and analysis system is not shown.

Z / N \* \* C O S F S / M M D L U T H I G G D D 3

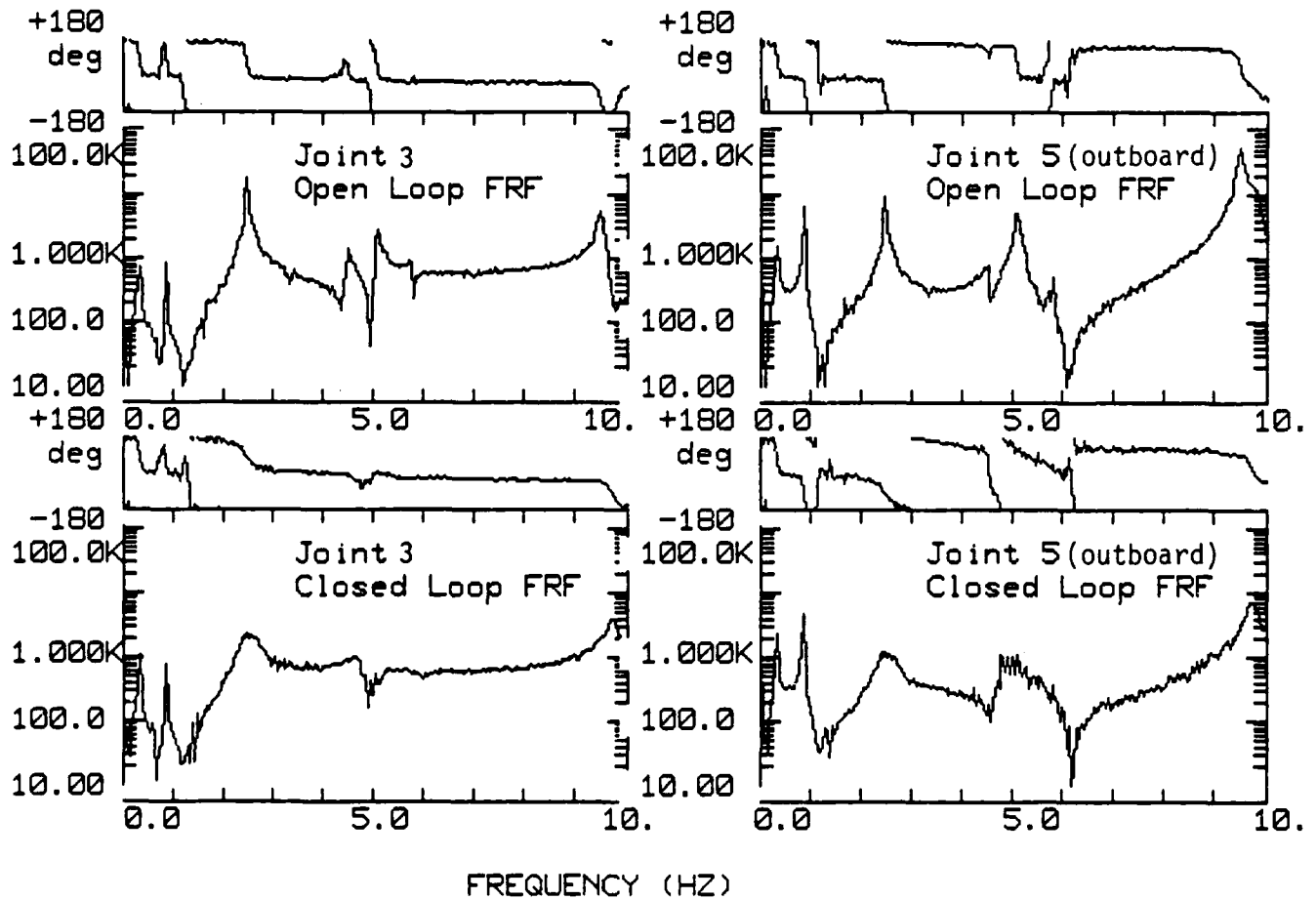


Fig. 35 Example acceleration/force frequency response functions for the slewing grid without (open loop) and with active damping. Excitation was generated by the force actuator on the DWD member (see Fig. 20).

END

DATE

FILMED

5-88

DTIC